# Strong Interaction between Platinum Nanoparticles and Tantalum-Doped Tin Oxide Nanofibers and Its Activation and Stabilization Effects for Oxygen Reduction Reaction

Ignacio Jiménez-Morales, Fatima Haidar, Sara Cavaliere, Deborah J Jones, Jacques Roziere

# Strong Interaction Between Platinum Nanoparticles and Tantalum Doped Tin Oxide Nanofibers and Its Activation and Stabilization Effect for Oxygen Reduction Reaction

*Ignacio Jiménez-Morales*[a, ‡], *Fatima Haidar*[a, ‡], *Sara Cavaliere*[a, b, *], *Deborah Jones*[a], *Jacques Rozière*[a]

[a] ICGM Université de Montpellier, CNRS, ENSCM, 34095 Montpellier Cedex 5, France.

[b] Institut Universitaire de France (IUF), 75231 Paris Cedex 5, France.

ABSTRACT: Electrocatalyst supports stable to high potential are required for the proton exchange membrane fuel cell cathode. Electrocatalyst supports based on tantalum doped tin oxide (Ta: $SnO_2$) were prepared by electrospinning. The dopant amount was varied between 0 (undoped $SnO_2$, TO) and 7.5 at.%, and the resulting materials were characterized for their morphology, composition, structure, porosity and electrical properties. Platinum nanoparticles prepared by a microwave assisted polyol method were deposited with different loadings on 1 at.% Ta doped $SnO_2$ (1Ta:SnO2), selected for its highest electrical conductivity of 0.09 S $cm^{-1}$. Their electrocatalytic properties towards the oxygen reduction reaction (ORR) were compared with those of the same

particles deposited on carbon black and those of a commercial carbon supported Pt catalyst. Pt/1Ta:$SnO_2$ showed higher ORR activity and stability at high potential than Pt/C. In particular, the electrocatalyst with the lowest Pt loading (7 wt%) presented high mass activity and stability which, from XPS analysis, is suggested to result from very strong metal support interaction. These results indicate that amongst tin oxides doped with pentavalent metals such as niobium (Nb:$SnO_2$), antimony (Sb:$SnO_2$) and tantalum, Ta:$SnO_2$ has the advantage of both higher conductivity than Nb:$SnO_2$, and greater stability in the fuel cell voltage range than Sb:$SnO_2$.

KEYWORDS: Electrocatalysis, alternative supports, tin oxide, strong metal support interaction, corrosion resistant supports.

## 1. INTRODUCTION

State-of-the-art cathodes of proton exchange membrane fuel cells (PEMFC) are based on Pt nanocatalysts supported on high surface area carbons. Great advances have been made in the fundamental understanding and experimental development of electrocatalysts aimed at reducing the noble metal content [1]. However, Pt-based catalysts supported on carbonaceous materials suffer from stability issues due to carbon corrosion at the potentials as high as 1.5 V (*vs* RHE) experienced by the cathode *e.g.* in start/stop conditions [2]. This leads to decrease in the surface area of the support with subsequent sintering and detachment of the catalyst particles [2,3]. The search for corrosion resistant materials meeting the electrocatalyst support requirements, including high electrical conductivity, porosity, and surface area, represents a great challenge for the development of durable PEMFC cathodes. With this aim, a range of materials and chemical compositions have been investigated, from graphitized carbons and conducting polymers to

transition metal nitrides, carbides, borides and oxides [4–7]. Electrocatalysts deposited on nanostructured transition metal oxides have demonstrated high electrochemical stability at high potential [8–12] with good electroactivity, which was attributed to their strong electronic interaction with these supports [13–15]. Tin oxide has been widely considered as an alternative to carbon [16,17] due to its high conductivity compared to other metal oxides, due to the presence of oxygen vacancies and non-stoichiometric $SnO_{2-\delta}$ [18]. In order to increase its conductivity, tin oxide is mostly employed in composites with carbon *e.g.* as a protecting layer preserving the conductivity of the support [19–21] or n-doped with pentavalent ions [22] including niobium [23–28] and antimony [15,24,36–38,26,29–35] providing an extra electron as charge carrier.

Several studies have established antimony doped tin oxide ($Sb:SnO_2$) as a promising support. It presents higher electrical conductivity than the niobium doped ($Nb:SnO_2$) counterpart, of the same order of that of carbon ($10^{-1}$ - 1 S $cm^{-1}$ at 20 °C [29,30,32,34,35,37]) combined with a remarkable stability to electrochemical corrosion that extends its utilization to applications where potentials even higher than 1.5 V *vs* RHE are reached [39,40]. The chemical stability of $Sb:SnO_2$ has been investigated in the wide range of potentials achievable during PEMFC operating conditions, revealing limitations strongly related to surface segregation of antimony. Significant leaching of antimony has been detected at very high potentials (> 1.9 V *vs* RHE), which is not relevant for the targeted application, but also at potentials as low as 0.4 V *vs* RHE. Different stability limits have been reported for $Sb:SnO_2$ materials and related to the different synthesis conditions.[24,32,36,41].

To overcome the drawbacks of $SnO_2$ doped with Nb and Sb, doping with tantalum (of ionic radius similar to those of Sn(IV), Nb(V) and Sb(V)) [18] has already led to highly conducting and stable materials [18,42]. Catalyzed with Pt nanoparticles, tantalum doped tin oxide ($Ta:SnO_2$) fused aggregated structures demonstrated greater activity than commercial Pt/carbon black in

rotating disk electrode (RDE) testing [43], also transposed in membrane-electrode assembly (MEA) characterization [44] with low noble metal loading [45].

The morphology of the tin oxide materials also plays a role, by affecting the catalyst layer structure and thus proton, electron and gas transfer. Therefore, specific synthesis [46] and deposition [45] methods of $SnO_2$ nanomaterials are being developed to control its porosity and architecture. With this aim, our group developed tin oxide supports by electrospinning, giving rise to fiber-in-tubes nanostructures with inter-grain, inter-fiber and intra-fiber porosity. The limits of these support materials in terms of electronic conductivity (Nb:$SnO_2$) [28,47] and potential window of stability (Sb:$SnO_2$) [40,48] were highlighted. Here, we describe the preparation of electrospun $SnO_2$ fibers doped with another pentavalent ion, tantalum (Ta:$SnO_2$). In particular, the doping degree was varied and optimized with regards to electrical conductivity and surface area. Ta:$SnO_2$ fibers were used to support two different loadings of Pt nanoparticles synthesized by a microwave assisted polyol method. This work presents the physico-chemical and electrochemical characterization of Ta:$SnO_2$-based electrocatalysts and an outlook for the development of ceramic supports for PEMFC.

## 2. EXPERIMENTAL

### 2.1 Preparation of Ta:$SnO_2$ nanofibers

Tantalum doped $SnO_2$ (Ta:$SnO_2$) fibers were prepared by electrospinning according to previously reported syntheses of similar materials[15,37,49]. 0.017 to 0.124 g of $TaCl_5$ (99 %, Sigma-Aldrich), corresponding to doping levels between 0 (undoped $SnO_2$) and 7.5 at.%, were added to a solution of 1.04 g of $SnCl_2$ (98 %, Sigma-Aldrich) and 0.9 g of polyvinylpyrrolidone

(PVP, average Mw ~ 1,300,000, Sigma-Aldrich) solution in ethanol (99.8 %, Fluka)/ N,N-dimethyl formamide (DMF, 98 % min., Fluka) = 1.8. The mixture obtained was stirred for 48 h to obtain a homogeneous solution that was electrospun at 20 °C on a rotating drum (Linari Nanotech) using an applied voltage of 15 kV (auto-reversing high voltage power supply Spellman CZE1000R), a needle-collector distance of 10 cm and a flow rate of 0.3 mL $h^{-1}$ (KDS 100 Legacy syringe pump, KD Scientific). The as-prepared $TaCl_5$-$SnCl_2$/PVP fibers were calcined at 600 °C for 4 h in air at a heating rate of 5 °C $min^{-1}$ to remove the carrier polymer and to allow formation of the fully inorganic fibers. The resulting samples were labelled x$Ta:SnO_2$ where x indicates the atomic concentration of tantalum dopant ranging from 0.5 to 7.5 at.%.

### 2.2 Preparation of Pt/$Ta:SnO_2$

A microwave-assisted polyol method [50] was used for the preparation of Pt catalyst nanoparticles. In a typical experiment, hexachloroplatinic acid (67 mg, 99.9 % Alfa Aesar) was dissolved in ethylene glycol (EG, 108 mL, 99.8 %, Sigma Aldrich) and the pH was adjusted to 11.2 with NaOH (1 M solution in EG). The solution obtained was heated at 165 °C for 4 minutes at 160 W in a microwave reactor (MiniFlow 200SS Sairem). The Ta doped-$SnO_2$ was added to the resulting Pt nanoparticle suspension to achieve a low (*ca* 10 wt.%) and high (*ca* 35 wt.%) Pt loading on the synthesized support materials after lowering the pH to 2 using $H_2SO_4$ (1 M solution in EG). The suspension was stirred for 48 hours, and then the Pt/$Ta:SnO_2$ was recovered by filtration, washed with Milli-Q® grade water and ethanol, and dried at 80 °C for 24 h. Further thermal treatment at 160 °C for one hour was performed to remove any traces of EG or its degradation products from the Pt surface. The same procedure was carried out for the preparation of Pt nanoparticles deposited on Vulcan XC-72R carbon black (Cabot) by adding 60 mg of support to the previously synthesized Pt nanoparticle suspension to achieve a Pt loading of *ca* 30 wt.% for

comparison of electrochemical activity and stability with the Ta:$SnO_2$ based electrocatalysts. The samples were labelled yPt/xTa:$SnO_2$ and yPt/Vulcan where y indicates the Pt loading (wt%) on Ta:$SnO_2$ fibers and carbon black, while x refers to the Ta at.%.

### 2.3 Physico-chemical characterization of Ta:$SnO_2$ and Pt/Ta:$SnO_2$

The morphology of Ta:$SnO_2$ and Pt/Ta:$SnO_2$ was analyzed using a Hitachi S-4800 scanning electron microscope (SEM), a FEI Quanta FEG 200 equipped with energy-dispersive X-ray spectroscopy (EDS) analysis and a JEOL 1200 EXII transmission electron microscope (TEM) operating at 120 kV, equipped with a CCD camera SIS Olympus Quemesa (11 million pixels). For TEM analysis the samples were suspended and sonicated (VWR Ultrasonic Cleaner) in ethanol, then deposited onto carbon-coated copper grids. The average sizes of Pt and Ta:$SnO_2$ materials were determined by measuring 200 selected objects using the ImageJ software.

Powder X-ray diffraction (XRD) patterns were recorded at 20 °C in Bragg-Brentano configuration using a PANalyticalX'pert diffractometer, equipped with a hybrid monochromator, operating with $CuK_\alpha$ radiation ($\lambda$ = 1.541 Å). A step size of 0.1° 2$\theta$ within the 2$\theta$ domain from 20 to 70 °.

X-ray fluorescence (XRF) analysis was used to determine the tantalum content of Ta:$SnO_2$ and the Pt loading on Pt/Ta:$SnO_2$. For analysis of Ta, 50 mg of sample were analyzed as flat pellets (8 mm diameter) by pressing powdered material at 2.2 tons for 5 min. A calibration line was obtained after carrying out a similar procedure for the preparation of five standards ranging from 0 to 8 at.% of $Ta_2O_5$ (99 wt.%, Sigma Aldrich) and $SnO_2$. For analysis of Pt, samples were prepared by grinding 50 mg of supported electrocatalyst with 25 mg of cellulose. The powder was placed in a cavity in an $H_3BO_3$ matrix and subsequently pressed to obtain a pellet of 32 mm diameter with scanned surface of *ca*. 12 mm. The same protocol was used to prepare eight standards using 5, 10,

15, 20, 25, 30, 35 and 40 wt% of Pt black (Alfa Aesar) and Ta:$SnO_2$ to obtain a calibration line. The XRF analyses were performed with a PANalytical Axios Max spectrometer fitted with a Rh (4 kW) tube, and equipped with a LiF200 crystal and Omnian software.

Nitrogen adsorption/desorption isotherms on Ta:$SnO_2$ materials were determined at -196 °C by means of a Micromeritics ASAP 2020 apparatus after outgassing overnight at 200 °C under vacuum ($10^{-3}$ Pa). The specific surface area ($S_{BET}$) was calculated by using the Brunauer-Emmett-Teller (BET) equation and taking 0.162 $nm^2$ as the cross-sectional area of one $N_2$ molecule. The pore-size distribution was calculated from the adsorption branch of the adsorption-desorption isotherms by the Barrett-Joyner-Halenda (BJH) equation.

The electronic conductivity of Ta:$SnO_2$ (in form of pellets as prepared for XRF analysis) was determined at 20 °C from resistance measurements carried out using a conductivity cell equipped with four gold electrodes and using the Van der Pauw calculations.

Raman spectroscopy analysis of Ta:$SnO_2$ fibers was performed on a LabRAM Aramis IR2 (Horiba Jobin Yvon) equipped with a blue laser diode ($\lambda$ = 473 nm, 17 mW on doped tin oxide) and a long working distance objective × 50.

The surface chemical state of the materials was investigated by X-ray photoelectron spectroscopy (XPS) on an ESCALAB 250 (Thermo Electron). The X-ray excitation was provided by a monochromatic Al $K_\alpha$ (1486.6 eV) source and the analyzed surface area was 400 $\mu m^2$. A constant analyzer energy mode was used for the electron detection (20 eV pass energy). Detection of the emitted photoelectrons was performed perpendicular to the sample surface. Data quantification was performed in the Avantage software, removing the background signal using the Shirley method. The surface atomic concentrations were determined from photoelectron peak

areas using the atomic sensitivity factors reported by Scofield. Binding energies of all core levels are referred to the C-C bond of C 1s at 284.8 eV.

### 2.4 Electrochemical characterization of Ta:$SnO_2$ and Pt/Ta:$SnO_2$

The electrochemical analyses were carried out at 20 °C using a Pine bipotentiostat model AFCBP1 in a conventional three-electrode cell composed of a reversible hydrogen electrode (RHE, reference electrode), a glassy carbon rotating disk electrode (RDE, (working electrode, geometric area 0.196 $cm^2$) and a platinum wire (counter electrode). All the potential values are referred to the RHE and the current densities are reported as current per geometric electrode area. To prepare the catalyst ink, 3 mg of 7-34Pt/1Ta:$SnO_2$ electrocatalyst were dispersed in 83.8-423,6 µL of Milli-Q grade water, 251.5-1271 µL of ethanol (Aldrich) and 17.1 µL 5 wt% Nafion® EW1100 solution in alcohols (Aldrich). For the references, 3 mg of 56.7 wt% Pt/C (HiSPEC 9100 from Johnson Matthey, 2.6 nm particle size measured by TEM) and 3 mg of 30 wt% Pt/Vulcan (Pt nanoparticles deposited on carbon black Vulcan XC-72R (Cabot)) were mixed, respectively, with 568 and 373.3 µL of Milli-Q grade water, 2.3 and 1.12 mL of ethanol (Aldrich) and 17.1 µL of a 5 wt% Nafion® EW 1100 solution in alcohols (Aldrich). Catalyst inks were sonicated (VWR Ultrasonic Cleaner) for 9 min and 7 µL aliquots were deposited onto the RDE surface with a micropipette and dried in air. The Pt loading onto the electrode was 21.3 µg $cm^{-2}$ for all electrocatalysts.

Cyclic voltammetry (CV) was performed in $N_2$ saturated 0.1 M $HClO_4$. The electrochemical surface area (ECSA) was calculated based on hydrogen desorption peaks in the range 0.05 V to 0.4 V *vs* RHE after double-layer correction, assuming a monolayer hydrogen adsorption charge of 210 µC $cm^{-2}$ for the Pt surface. For the accelerated stress tests specifically probing the corrosion resistance of the support, 6,000 cycles were performed between 1.0 V and 1.6 V *vs* RHE with a

scan rate of 100 mV $s^{-1}$ [51]. Every 100 cycles, one cycle between 0.025 V and 1.2 V with a scan rate of 20 mV $s^{-1}$ was performed to determine the ECSA and evaluate its decay over the high-voltage cycling. The ORR curves were recorded using linear sweep voltammetry at 1,600 rpm in $O_2$ saturated 0.1 M $HClO_4$, varying the potential from 0.1 V to 1.2 V *vs* RHE at a scan rate of 20 mV $s^{-1}$. All the ORR curves performed in $O_2$-saturated solutions were corrected by subtracting the background capacitive current obtained in an in $N_2$-saturated 0.1 M $HClO_4$. Previous to the measurements, the curves were also IR corrected (measure of the electrolyte resistance and compensation with 85 % of this value).

To assess the Pt electrocatalyst stability on 7Pt/1Ta:$SnO_2$, 10,000 cycles were performed between 0.6 V and 1.0 V *vs* RHE with a scan rate of 500 mV $s^{-1}$ [51]. Every 100 cycles, ECSA was evaluated.

Mass (MA) and specific activity (SA) values were calculated by dividing the kinetic currents obtained applying the Koutecky-Levich equation by the mass of Pt deposited onto the RDE or the Pt ECSA, respectively.

Potentiostatic accelerated stress tests (AST) were performed by holding the working electrode potential at 1.5/1.6/.7/1.8/1.9/2.0 V *vs* RHE for 4 hours in 0.5 M $H_2SO_4$ at 80 °C. The ink was prepared by dispersing 20 mg of 1Ta:$SnO_2$ in 4.29 mL ethanol/water solution (3/1 v/v) and 97.1 μL of 5 $\%_{wt.}$ Nafion® EW1100 dispersion in alcohols (Aldrich). After ultrasonication (VWR Ultrasonic Cleaner), the entire volume was deposited onto a Ti foil by manual spraying on a hot plate at 70 °C to remove the solvent. Inductively coupled plasma-mass spectroscopy (ICP-MS, Agilent 7900) measurements of 10 mL of the electrolyte solution after chronoamperometry were performed after addition of 1 mL of *aqua regia* to dissolve any solids. During the experiment the electrolyte was not exchanged, therefore the dissolved elements accumulated. The reported

concentration values for every applied potential were obtained by subtracting those measured in the precedent steps.

## 3. RESULTS AND DISCUSSION

### 3.1 Morphological, structural and textural characterization of electrospun Ta:$SnO_2$

The chemical composition of the tin oxide materials prepared using different amounts of tantalum, determined by XRF and SEM-EDX analysis, is provided in

Table **1**. The results obtained with the two techniques are consistent and in agreement with the nominal amount of Ta.

**Table 1.** Ta content (Ta at.%) in Ta:$SnO_2$ materials obtained by XRF and SEM-EDX analyses.

| **Sample** | **Ta at.%** | | |
|---|---|---|---|
| | **Nominal** | **XRF** | **SEM-EDX** |
| 0.5Ta:$SnO_2$ | 0.5 | 0.51 | 0.53 |
| 1Ta:$SnO_2$ | 1.0 | 1.02 | 1.04 |
| 1.5Ta:$SnO_2$ | 1.5 | 1.51 | 1.52 |
| 2Ta:$SnO_2$ | 2.0 | 1.98 | 2.01 |
| 5Ta:$SnO_2$ | 5.0 | 5.05 | 4.88 |
| 7.5Ta:$SnO_2$ | 7.5 | 7.48 | 7.43 |

SEM analysis was carried out to investigate the morphology of the electrospun materials bearing different amounts of tantalum (Figure 1). All samples had fibrous porous structures, formed by

primary nanoparticles. On increasing the Ta content, the morphology progressively evolved from dense fibers to fiber-in-tubes at 1.5 at.% Ta. Such morphology was observed previously when doping electrospun $SnO_2$ with Nb and Sb [15,49]. In particular, the conditions of this morphological transition were investigated and interpreted for Nb doped $SnO_2$ [49] and ascribed to the presence of the doping agent *via* the diffusion of the dopant to the outer structure [52,53]. In this work, tantalum is seen to drive the formation of fiber-in-tubes above the 1.5 at.% threshold. The average diameters of the Ta:$SnO_2$ fibers/tubes increased with increasing the Ta amount, from 138 nm (0.5Ta:$SnO_2$) to 170 nm (7.5Ta:$SnO_2$) (Figure S1, Supporting Information). In contrast, as evidenced by TEM analysis, the size of the primary particles composing the fibrous materials progressively decreased with Ta concentration, from 18 nm (0.5Ta:$SnO_2$) to 8 nm (7.5Ta:$SnO_2$) (**Figure 2** and Figure S2, Supporting Information), in agreement with the particle growth inhibition promoted by the presence of the doping agent in tin oxide [54].

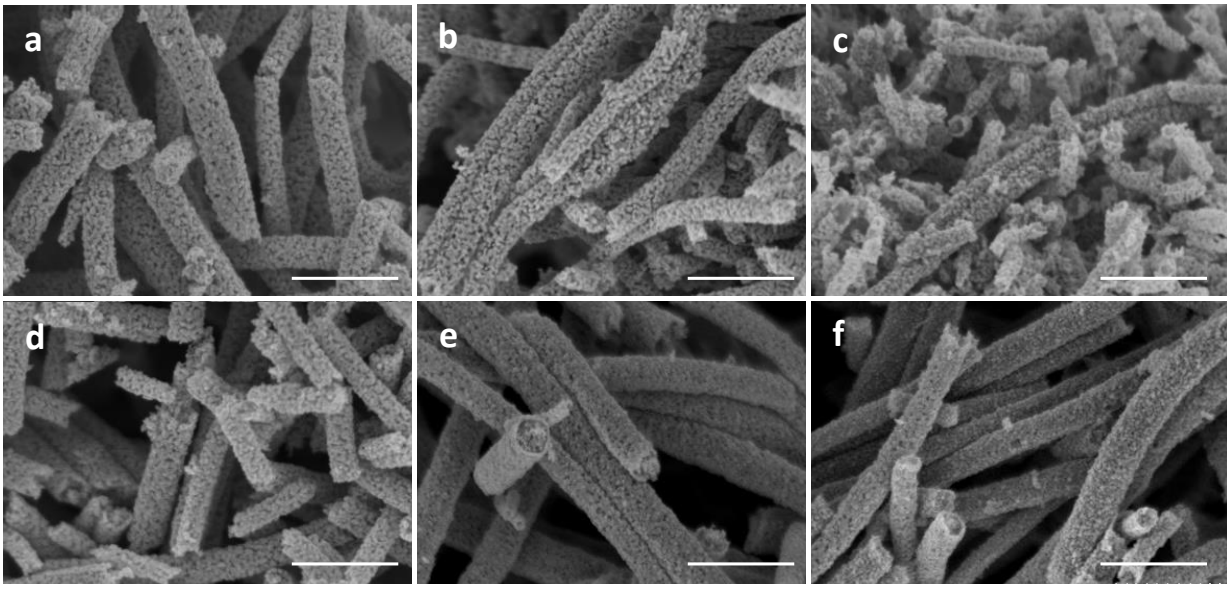


**Figure 1.** SEM micrographs of 0.5Ta:$SnO_2$ (a), 1Ta:$SnO_2$ (b), 1.5Ta:$SnO_2$ (c), 2Ta:$SnO_2$ (d), 5Ta:$SnO_2$ (e) and 7.5Ta:$SnO_2$ (f). The scale bars correspond to 600 nm.

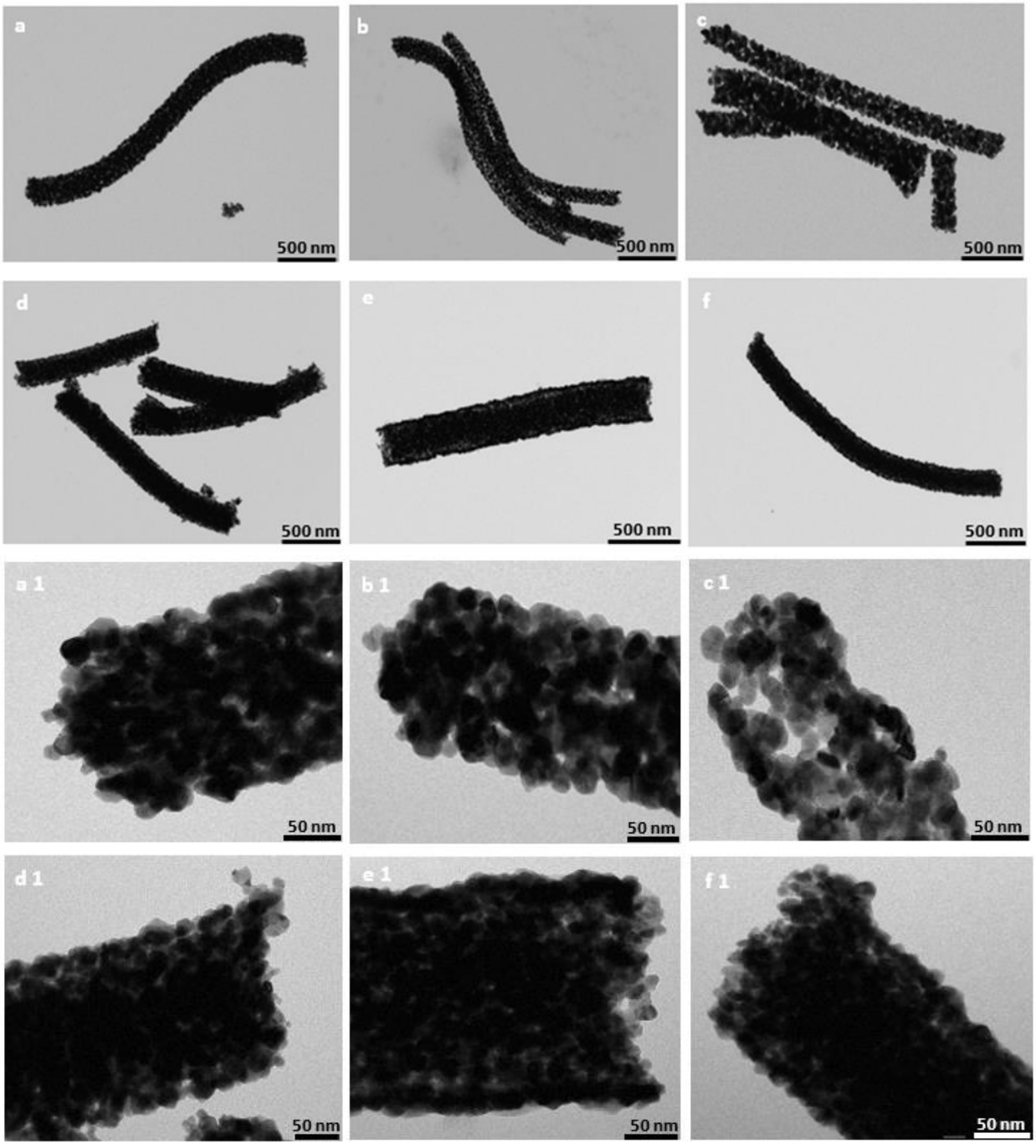


**Figure 2.** TEM micrographs of 0.5Ta:$SnO_2$ (a, a1), 1Ta:$SnO_2$ (b, b2), 1.5Ta:$SnO_2$ (c, c1), 2Ta:$SnO_2$ (d, d1), 5Ta:$SnO_2$ (e, e1) and 7.5Ta:$SnO_2$ (f,f1).

XRD diffractograms for Ta:$SnO_2$ materials with different Ta doping levels are depicted in Figure 3. Similar diffractions peaks were obtained for all electrospun materials, which can be indexed to polycrystalline tetragonal P42/*mnm* rutile cassiterite $SnO_2$ structure (JCPDS 41-1445). No evidence for segregated tantalum/tantalum oxide phases was detected at any of the doping levels investigated.

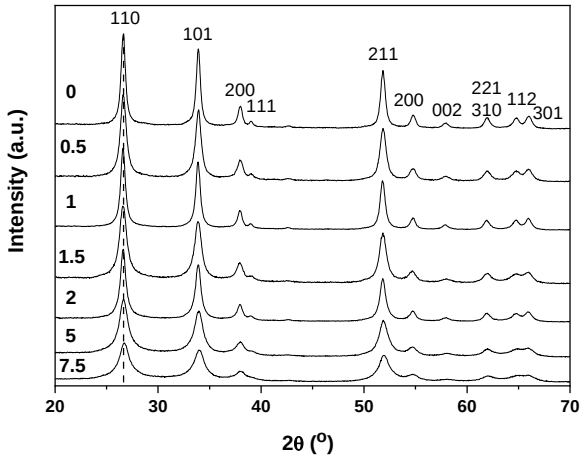


**Figure 3.** XRD diffraction patterns for undoped and doped tin oxide with the Ta at.% indicated in the figure (0-7.5 at%).

This confirms a homogeneous distribution of tantalum(V) ions in the $SnO_2$ lattice (rather than a mixture of the respective oxides), which is facilitated by their similar ionic radius and electronic configuration [18]. The varying Ta doping level led to two main structural effects observed in the diffractograms: (i) By increasing the tantalum atomic concentration the diffraction peaks broadened, indicating a decrease in the average crystallite size, estimated from the Scherrer equation as 18.6 nm for 0.5Ta:$SnO_2$ to 8.7 nm for 7.5Ta:$SnO_2$ (Table 2). These results are in agreement with TEM observations (Figure S2, Supporting Information) and with the known phenomenon of particle growth inhibition ascribed to the doping agent in metal oxides [12,15];

(ii) Diffraction peaks slightly shifted to lower 2θ positions on increasing tantalum doping levels up to 2 at.% (from 26.7 to 26.6 °), while at higher Ta contents the diffraction peaks were observed at their initial position (and even at slightly higher, 26.8 °, at 7.5 at.%). The shift to lower angles of XRD lines at increasing level of Ta indicates an increase of the unit cell volume, which is in agreement with the slightly higher ionic radius of $Ta^{5+}$ (0.73 Å) than that of $Sn^{4+}$ (0.69 Å), and which is consistent with the insertion of $Ta^{5+}$ into the $SnO_2$ lattice.

Raman spectroscopy was also used to assess the effect of Ta doping on distortion of the $SnO_2$ rutile structure. Raman spectra of undoped and doped $SnO_2$ electrospun materials are reproduced in Figure 4. No lines at wavenumbers characteristic of $Ta_2O_5$ [55,56] were detected in the whole set of samples, in agreement with XRD results, confirming the tin substitution with tantalum. For all the samples, peaks centered at 630 and 772 $cm^{-1}$ are observed, which can be attributed to the $A_{1g}$ and $B_{2g}$, fundamental modes of tetragonal rutile [57]. $E_g$ fundamental modes at 470 $cm^{-1}$ are barely visible as overlapped with other features. As the tantalum atomic concentration was increased up to 2 at.%, the $A_{1g}$ band progressively broadens and shifts to lower wavenumbers, however returned to the same frequency at higher Ta contents. At the same time, the $B_{2g}$ (and $E_g$) modes shift and merge with $A_{1g}$, being barely distinguishable at Ta concentrations greater than 1.5 at.%. The redshift and broadening of the active modes correspond to the phonon confinement effect due to decrease in primary particle size [58–66]. Another effect of the increase in Ta concentration in $SnO_2$ up to 2 at.% is the appearance of lines from Raman-forbidden modes in the range 250 to 700 $cm^{-1}$. The appearance of these lines indicates lowering of crystal symmetry (disorder, defects) and confinement-induced relaxation of selection rules [60–66] due to the decrease in crystal size induced by the doping agent. For higher Ta concentrations (5 and 7.5 at.%), the intensity of the forbidden modes decreased, indicating a return to a more ordered structure.

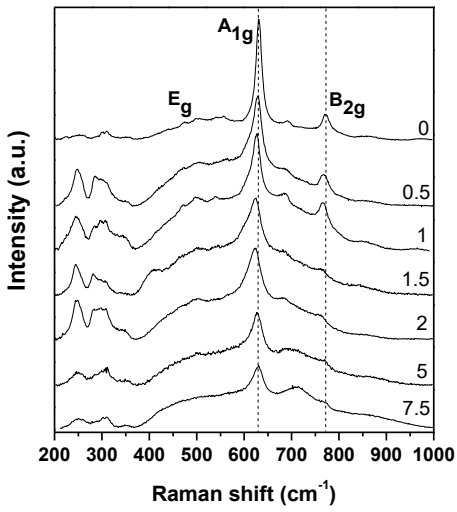


**Figure 4.** Raman spectra of tin oxide fibers doped with 0-7.5 at.% Ta.

Nitrogen adsorption-desorption isotherms were recorded to determine the influence of Ta dopant concentration on the specific surface area and porosity of Ta:$SnO_2$. The isotherms, (Figure S3a, Supporting Information), show hysteresis in the relative pressure range of 0.7–1.0, which is sorption behavior typical of mesoporous materials, type IV according to the IUPAC classification [67]. The calculated pore size distribution (PSD) is depicted in Figure S3b. On increasing the tantalum content, a significant increase in the BET surface area was observed, with a decrease in average pore size (Figure S3b) and pore volume (Table 2). Furthermore, the PSD evolved from bimodal (centered at 14 and 28 nm) to monomodal (centered at 14 nm from 5 at.%). This evolution can be correlated to the trend in the size of nanoparticles composing the Ta:$SnO_2$ fibers, which decreases on increasing Ta content, implying that the developed porosity is due to intrafiber and interparticle surfaces. Similar results were observed for vanadium [68] and tantalum [46] doped-$SnO_2$ nanomaterials.

**Table 2.** Textural parameters obtained from nitrogen adsorption/desorption isotherms and average crystallite obtained by XRD analysis size for undoped and doped tin oxide (xTa:$SnO_2$) materials.

| Sample | $S_{BET}$ ($m^2 \cdot g^{-1}$) | Pore volume ($cm^3 \cdot g^{-1}$) | Average pore size (nm) | Crystallite size (nm) (XRD) |
|---|---|---|---|---|
| $SnO_2$ | 20 [49] | n.d. | n.d. | 19.4 |
| 0.5Ta:$SnO_2$ | 24 | 0.167 | 24 | 18.6 |
| 1Ta:$SnO_2$ | 27 | 0.153 | 23 | 17.6 |
| 1.5Ta:$SnO_2$ | 30 | 0.145 | 21 | 16.3 |
| 2Ta:$SnO_2$ | 32 | 0.136 | 19 | 14.7 |
| 5Ta:$SnO_2$ | 58 | 0.114 | 14 | 9.9 |
| 7.5Ta:$SnO_2$ | 63 | 0.109 | 12 | 8.7 |

n.d. not determined

### 3.2 Surface analysis of Ta:$SnO_2$ fibers

High resolution XPS spectra of Sn 3d and Ta 4d core levels are depicted in Figures 4a and 4b, respectively. XPS of tantalum is usually approached through the Ta 4f level (at 22–24 eV) since it gives rise to the most intense signal. However, in presence of Sn, Ta 4f emission peaks are hidden by the stronger emission (at about 25 eV) from Sn 4s [69]. Therefore, the Ta 4d emission line was used to investigate the chemical state and the concentration of tantalum in Ta:$SnO_2$ samples. The peak positions of Sn $3d_{5/2}$ and Sn $3d_{3/2}$ (486.6 and 495.0 eV) and spin-orbit splitting of 8.4 eV correspond to Sn(IV) [52,70]. The presence of $Sn^{2+}$ on the material surface cannot nevertheless be excluded [49], due to the intrinsically oxygen-deficient structure of $SnO_2$ [18,71]. Considering the binding energies of the doublets (230.4 and 242.0 eV) and the spin-orbit splitting at 11.6 eV, the Ta $4d_{5/2}$ and Ta $4d_{3/2}$ peaks can be assigned to Ta(V) [72]. Ta/Sn atomic ratios calculated by integration of the XPS peaks (Table 3) were in agreement with the values obtained by XRF and SEM-EDS (

Table **1**).

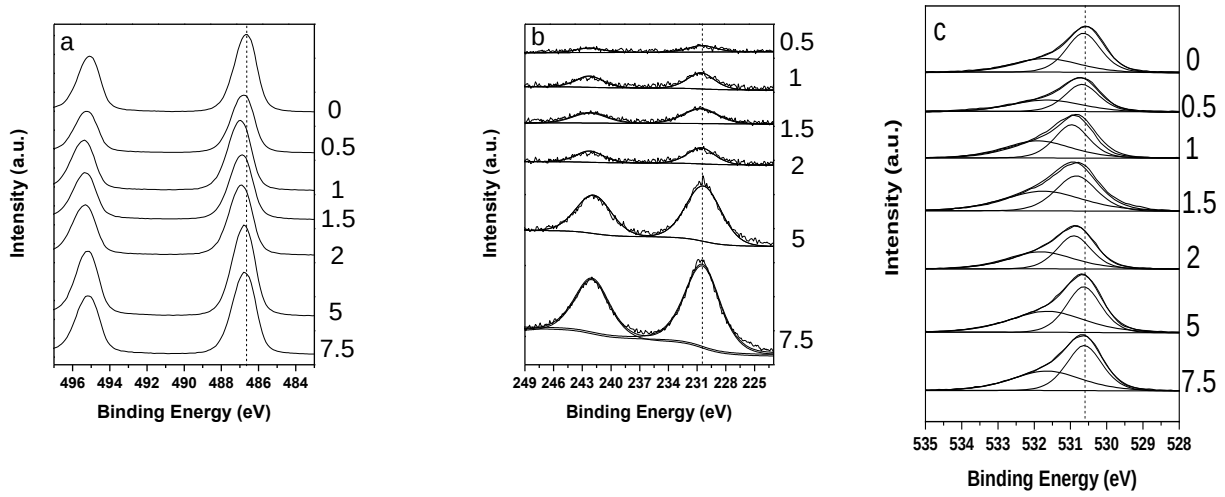


**Figure 4.** XPS core level spectra of Sn 3d (a), Ta 4d (b) and O 1s (c) for of tin oxide fibers doped with 0-7.5 at.% Ta.

This result indirectly indicates that Ta is homogeneously distributed through the material and is not segregated at the surface or within the inner part of the fiber (as in Sb [48] and Nb [49] doped electrospun tin oxides).

**Table 3.** XPS derived Ta/Sn and O/Ta+Sn atomic ratios for electrospun Ta:$SnO_2$.

| **Sample** | **Ta/Sn** | **O/Ta+Sn** |
|---|---|---|
| $SnO_2$ | - | 1.25 |
| 0.5Ta:$SnO_2$ | 0.0054 | 1.33 |
| 1Ta:$SnO_2$ | 0.0106 | 1.37 |
| 1.5Ta:$SnO_2$ | 0.0153 | 1.40 |
| 2Ta:$SnO_2$ | 0.0199 | 1.42 |
| 5Ta:$SnO_2$ | 0.048 | 1.44 |

7.5Ta:$SnO_2$ 0.073 1.45

Sn 3d doublets (Figure 4a) of Ta:$SnO_2$ undergo progressive shift to higher binding energy on increasing the amount of Ta in $SnO_2$ up to 5 at.%. For higher Ta concentrations, the peak position returned to the same value that for undoped tin oxide. Also, an increase in the peak asymmetry with the amount of tantalum was observed. These results are consistent with the observations of structural analysis (XRD, Raman spectroscopy), and might suggest that the shift toward higher binding energy is due to distortion of the rutile structure upon doping with increasing amounts of tantalum. Similar results have been already reported for structural changes induced by thermal treatment [60] or doping [15,73]. The O 1s high resolution spectrum for undoped $SnO_2$ (Figure 4c) exhibit a broad peak between 528 and 535 eV, which is deconvoluted into two contributions, a peak at 530.5 eV, assigned to $O^{2-}$ ions in the oxide lattice structure, and a peak at 531.6 eV to $H_2O$, OH or CO surface-adsorbed species [74,75]. A progressive shift of the oxide peak to higher binding energy was observed as the amount of dopant increased up to 5 at.%. For higher tantalum contents, the peak position was the same as for the undoped material. The O/Sn+Ta atomic ratio (Table 3) is lower than the expected value of 2, indicating oxygen vacancies in the tin oxide based materials [18,71], The O/Sn+Ta ratio increases as the tantalum content increases up to a value of 1.45 for 7.5 at.% Ta. This ratio never reached the expected value of 2 for stoichiometric $SnO_2$, which is compatible with the existence of oxygen vacancies. The latter decrease when increasing the Ta amount. It is worth to notice that the extremely low Sn/O ratio of 1.25 for the undoped oxide is not representative of its stoichiometry, but in agreement with the presence of oxygen deficient $SnO_2$, and $Sn^{2+}$ at the surface (XPS analysis) [49].

### 3.3. Electrical conductivity of Ta:$SnO_2$ fibers

Electrical conductivity measurements were carried out on all the samples with Ta content ranging from 0 to 7.5 at.% (Figure S4, Supporting Information). The conductivity increased (from 1.1 $10^{-3}$ S $cm^{-1}$ for undoped $SnO_2$) by increasing the degree of doping, to reach a maximum value of 0.09 S $cm^{-1}$ at 1 at.%. Similar results were obtained for Nb and Sb doped electrospun $SnO_2$ where the maximum conductivity was obtained for 5 at.% Nb (0.02 S $cm^{-1}$) and 10 at.% Sb (1.02 S $cm^{-1}$), respectively [37,49]. Further increase in the carrier concentration led to a decrease in conductivity due to a decrease in their mobility [71]. The higher conductivity of tantalum than niobium doped $SnO_2$ was reported previously for doped $SnO_2$ nanoparticles and films [43,76]. Due to the different measurement methods used, the absolute values of these electrical conductivity values cannot be compared (of the order of $10^{-4}/10^{-3}$ S $cm^{-1}$ for the nanoparticles and $10^2/10^3$ for the films). These results suggest that the higher electrical conductivity determined for 1Ta:$SnO_2$ may be correlated to the maximum distortion and/or defects in $SnO_2$ rutile structure indicated by the structural and surface analyses described above.

This trend in electrical conductivity is consistent with values predicted by DFT calculations and confirmed by experimental data for Ta:$SnO_2$ thin films by Worsdale *et al.* [76], where the maximum conductivity at 1 at.% was ascribed to the limited dopant solubility and to the Jahn-Teller lattice distortion lowering the donor state with increasing dopant concentration.

Because of its highest electrical conductivity among the synthesized materials, 1Ta:$SnO_2$ was selected for further electrochemical characterization as electrocatalyst support.

### 3.4 Electrochemical stability of 1Ta:$SnO_2$

The corrosion current of Ta:$SnO_2$ was negligible, as expected for a metal oxide [12,20]. Ta:$SnO_2$ fibers were submitted to potential holds from 1.5 to 2 V *vs* RHE in acidic medium at 80 °C (Figure S5, SI). Oxidation currents were followed by chronoamperometry, while the support integrity was

evaluated by quantifying the release of Sn and Ta ions into the electrolyte by ICP-MS (Figure 5). For polarization at 1.6 V *vs* RHE, 0.1 μg $L^{-1}$ of Ta and 2.48 μg $L^{-1}$ of Sn were released. The loss of tantalum was ca. 2.6 times lower than the stoichiometric ratio (1:99) of the elements in 1Ta:$SnO_2$ (already validated by XRF, XPS and SEM-EDX). At the end of the experiment, 0.10 wt% of Ta was dissolved vs 0.021 wt% of Sn (see Table S1). The loss of elements into solution may result from Ta:$SnO_2$ detachment from the electrode as well as to a preferential loss of Sn. For 10 % Sb:$SnO_2$ fibers, we earlier determined [48] release at 1.6 V *vs* RHE of 5.5 μg $L^{-1}$ of Sb and 22.6 μg $L^{-1}$ of Sn, which (taking into account the different at.% of doping agent) demonstrates the higher stability of tantalum doped oxide compared to the antimony counterpart. The instability of Sb-$SnO_2$ was ascribed to the segregation of antimony at the surface of the material (which facilitates its dissolution and leads to a decrease in the electrical conductivity [77]), which has not been observed for Ta:$SnO_2$, which may explain its higher stability.

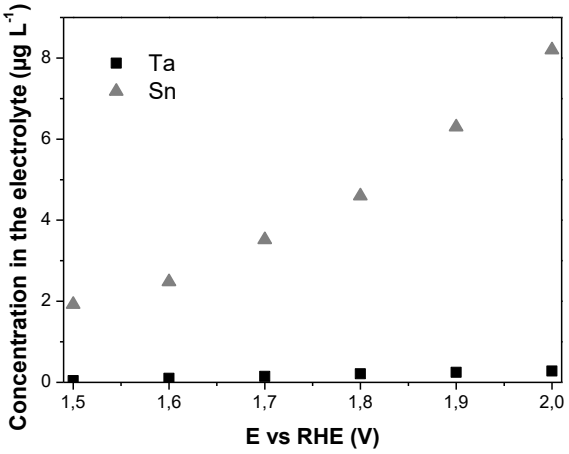


**Figure 5.** ICP-MS analysis of Sn and Ta detected in the electrolyte (0.5 M $H_2SO_4$) during the 4-hour chronoamperometry experiments at 80 °C from 1.5 to 2.0 V *vs* RHE.

### 3.5 Morphological and structural characterization of Pt/1Ta:$SnO_2$

Pt nanoparticles were synthesized by microwave assisted polyol method and deposited onto 1Ta:$SnO_2$ with loadings of 7 and 34 wt% and onto carbon Vulcan with a loading of 30 wt. % (determined by XRF and EDS analysis). TEM micrographs (Figures 6 and S6, Supporting Information) demonstrated a uniform dispersion of the metal particles on the supports, with an average diameter of 3.2 nm.

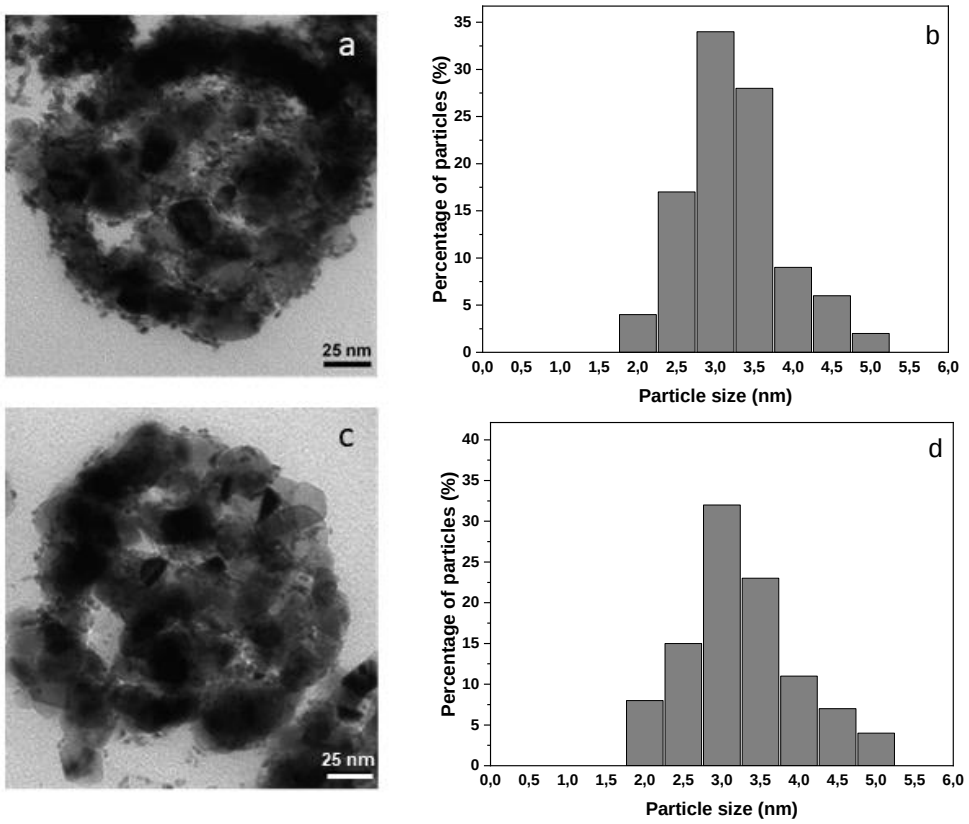


**Figure 6.** TEM micrograph and the corresponding Pt size distribution histograms of a) 34 % Pt/1Ta:$SnO_2$ (a, b) and 7 % Pt/1Ta:$SnO_2$ (c, d).

The XRD pattern of 34Pt/1Ta:$SnO_2$ (Figure S7, SI) confirms the presence of lines of the face-centered cubic structure of Pt (2θ = 39.7, 46.2 and 67.41, JCPDS 004-0802) in addition to the diffraction lines corresponding to tetragonal cassiterite $SnO_2$. In agreement with TEM results, the

average diameter size of Pt crystallites on Ta:$SnO_2$ calculated from the Scherrer equation on Pt(111) was 3.4 nm.

### 3.6 Surface analysis of Pt/1Ta:$SnO_2$

X-ray photoelectron spectroscopy (XPS) was carried out to investigate the surface chemical state of the Pt/1Ta:$SnO_2$ bearing different amounts of electrocatalyst. The analysis of Pt, Ta, Sn and O elements was performed. Figures 7c and d depict the XPS spectra of the Sn3d and Ta4d core level, respectively.

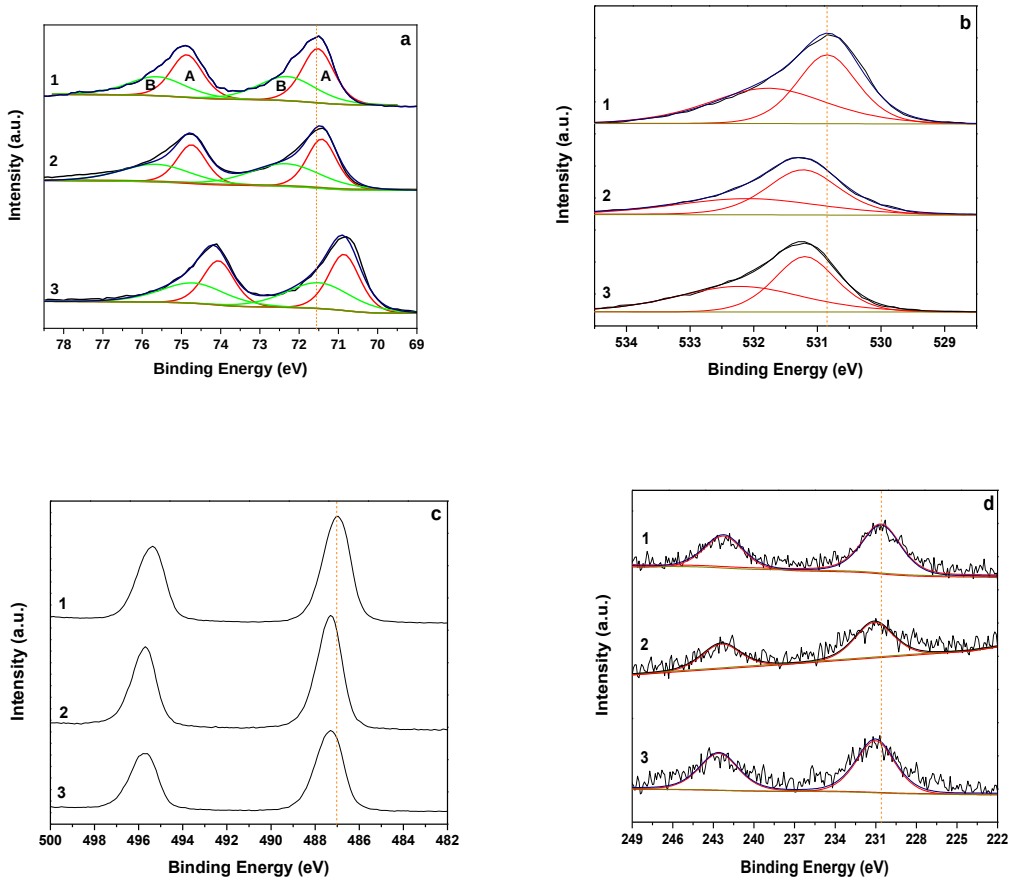


**Figure 7.** XPS core level spectra of a) Pt4f and b) O1s for 1) Pt/Vulcan, 2) 34Pt/1Ta:$SnO_2$ and 3) 7Pt/1Ta:$SnO_2$, c) Sn3d and d) Ta4d for 1) 1Ta:$SnO_2$ (Pt/Vulcan for Pt4f spectrum) 2) 34Pt/1Ta:$SnO_2$ and 3) 7Pt/1Ta:$SnO_2$.

The deposition of Pt nanoparticles on Ta:$SnO_2$ did not change the oxidation state of Sn and Ta (based on the binding energies of the doublets and spin-orbit splitting, see Table 4), however a shift to higher binding energy (+ 0.3 eV) was observed when compared to the non-catalyzed Ta:$SnO_2$.

**Table 4.** Binding energies (B.E.) values forPt 4f, O 1s, Sn 3d and Ta 4d for Pt/Vulcan, 1Ta:$SnO_2$, 34Pt/1Ta:$SnO_2$ and 7Pt/1Ta:$SnO_2$.

| **Sample** | **B.E. Pt 4f (eV)** | | **B.E. O1s (eV)** | **B.E. Sn 3d (eV)** | **B.E. Ta 4d (eV)** |
|---|---|---|---|---|---|
| | A 7/2 / 5/2 | B 7/2 / 5/2 | $O^{2-}$/$OH^-$, $H_2O$ | 5/2 / 3/2 | 5/2 / 3/2 |
| Pt/Vulcan | 71.6/74.9 | 72.4/75.7 | - | - | - |
| 1Ta:$SnO_2$ | - | - | 530.8/531.8 | 487/495.4 | 230.6/242.2 |
| 34Pt/1Ta:$SnO_2$ | 71.4/74.7 | 72.2/75.5 | 531.2/532.3 | 487.3/495.7 | 230.9/242.5 |
| 7Pt/1Ta:$SnO_2$ | 70.9/74.1 | 71.6/74.8 | 531.2/532.3 | 487.3/495.7 | 230.9/242.5 |

Similar results were obtained for O1s core level spectra displayed in Figure 7b, presenting a shift to 0.4 eV higher binding energy (Table 4). This effect has already been observed and attributed to the strong metal support interaction leading to a charge transfer from the oxide to platinum, inducing a local increase of the electron density on Pt [14,15]. In addition, an increased proportion of the O ($OH^-$, $H_2O$)/O ($O^{2-}$) is observed after deposition of Pt NPs, indicating their partial oxidation on the surface. In Figure 7a is displayed the Pt4f region of 7Pt/1Ta:$SnO_2$, 34Pt/1Ta:$SnO_2$ and Pt/Vulcan. Pt was present in metallic form since $Pt4f_{7/2}$/$Pt4f_{5/2}$ doublet was observed (A bands) and a second doublet at higher binding energy (B bands) was also present (Table 4) and related to $PtO_{ads}$ and/or $Pt(OH)_2$ [15,78] due to partial surface oxidation already demonstrated by the O 1s spectra. A downshift of 0.2 eV is noted comparing 34Pt/1Ta:$SnO_2$ to 30Pt/Vulcan in agreement with the Sn 3d, Ta 4d and O 1s XPS results discussed above, consistent with the SMSI hypothesis. It is known that n-doping in semiconductors leads to the creation of a donor level near the conduction band. As a result, the Fermi level moves upward, close to the conduction band, and the work function decreases [79]. According to the literature on SMSI, the supported metal phase has

a larger surface energy and work function and lower Fermi energy than the support [80,81]allowing electron transfer from the oxide (higher Fermi level) to the metal (lower Fermi level). In this work, such electron transfer is demonstrated by the binding energy shift on opposite directions of the $SnO_2$ and Pt core levels after the Pt deposition: the electron density increased on Pt (BE negative shift) and decreased on $SnO_2$ (BE positive shift). BE shifts were already reported for Pt/$SnO_2$ in some cases in opposite directions compared to the results of this work [14,82–84]. This may be due to a more complex description of the SMSI, involving not only charge transfer, but also changes in the lattice parameters [85] and interfacial alloy formation [83].

It is worth noting the enhanced downshift of 0.7 eV for 7Pt/1Ta:$SnO_2$, suggesting a stronger SMSI effect and electron transfer. This phenomenon may be ascribed to the more efficient contact area of isolated particles with the support due to the lower particle loading. The increased shift of Pt BE with decreasing metal loading has already been reported by Rabis *et al.* [82], who further related this phenomenon to an increased ORR activity.

### 3.7 Electrochemical characterization of Pt/1Ta:$SnO_2$

Cyclic voltammograms recorded on Pt/1Ta:$SnO_2$ samples with Pt loadings of 7 and 34 wt% in nitrogen-saturated $HClO_4$ presented the typical hydrogen adsorption/desorption peaks as well as oxide formation and reduction on platinum (Figure S8, Supporting Information). For comparison, the same characterization was performed on 30Pt/Vulcan prepared with the same protocol, and on HiSPEC 9100. The ECSA values were obtained based on the hydrogen desorption peaks. Very similar values were obtained for Pt on carbon (80 $m^2\ g^{-1}$ for the Pt/Vulcan and 78 $m^2\ g^{-1}$ for the HiSPEC 9100), in agreement with the surface areas calculated considering the Pt nanoparticle diameter. The ECSA for the Pt/1Ta:$SnO_2$ samples greatly depended on the Pt loading, being 48 $m^2\ g^{-1}$ for 34Pt/1Ta:$SnO_2$ and 73 $m^2\ g^{-1}$ for 7Pt/1Ta:$SnO_2$. The higher ECSA for the lower metal

loading may be ascribed to the better accessibility of the surface sites of the electrocatalyst due to the better dispersion on the support (isolated particles), considering its low developed surface area ($S_{BET}$ =27 $m^2 \cdot g^{-1}$). The ECSA of 7Pt/1Ta:$SnO_2$ is similar to that of Pt/Vulcan, where the Pt loading was 30 wt% on a higher surface support (*ca* 250 $m^2 \cdot g^{-1}$ for Vulcan vs 27 $m^2 \cdot g^{-1}$ for 1Ta:$SnO_2$). Past reports [23,25,34,35,43,86–89] indicated a large range of ECSA calculated for Pt deposited onto undoped and Nb/Sb/Ta doped tin oxide (18-84 $m^2 \cdot g^{-1}$). Further, the ECSA of 34Pt/1Ta:$SnO_2$, 48 $m^2$ $g^{-1}$, is the same as that of similar Pt catalyzed fiber-in-tubes prepared with otherwise identical method (33 wt.% Pt/Nb:$SnO_2$ and 37 wt.% Pt/Sb:$SnO_2$ (47 and 44 $m^2$ $g^{-1}$, respectively) [15]. It was considered that encapsulation of the metal particles associated with strong metal-support interaction could lower the ECSA [90]. In the light of the present results, the agglomeration of the nanosized catalysts due to the high loading compared to the low surface area of the support may also explain the reduced electroactive available sites and lower electrochemical specific surface area of the deposited Pt.

In Figure 8 are depicted the linear sweep voltammograms recorded in $O_2$-saturated 0.1 M $HClO_4$ on 7Pt/1Ta:$SnO_2$, 34Pt/1Ta:$SnO_2$, 30Pt/Vulcan and HiSPEC 9100. The corresponding Tafel plots are presented in Figure S9 (Supporting Information). The diffusion-limited current was lower for the high loaded 34Pt/1Ta:$SnO_2$ compared to the other electrocatalysts, which may indicate incomplete electrical contact of the catalyst with the support [88], possibly ascribed to the higher loading and consequent agglomeration of Pt particles.

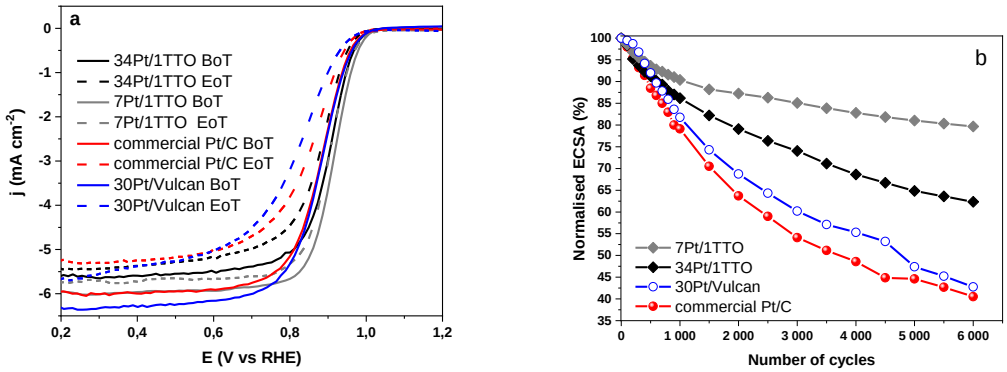


**Figure 8.** ORR polarization curves recorded at 1,600 rpm in $O_2$ saturated 0.1 M $HClO_4$, at a scan rate of 20 mV $s^{-1}$ (a) and ECSA variation (measured in $N_2$ saturated 0.1 M $HClO_4$, at a scan rate of 20 mV $s^{-1}$) upon electrochemical cycling up to 1.6 V *vs* RHE (b) for Pt nanoparticles deposited on 1Ta:$SnO_2$ (34 wt % Pt in black, 7 wt% in grey) and Vulcan (in blue) and for commercial Pt/C electrocatalyst (in red). The linear sweep voltammograms were recorded at the beginning and end of the accelerated stress test (BoT, full lines, and EoT, dotted lines).

The ORR mass (MA) and specific activity (SA) values at 0.9 V *vs* RHE of Pt deposited on the Ta doped $SnO_2$ fibers and on carbon black and HiSPEC 9100 are listed in Table 5. Pt/1Ta:$SnO_2$ electrocatalysts exhibited the highest specific and mass activities reported for Pt deposited on $SnO_2$ supports doped with Ta [43,45] or other heteroatoms [15,16,43,86,88,89,23–27,29,30,33]. The specific activity was the same for both Ta:$SnO_2$-based electrocatalysts (640 μA $cm^{-2}$) and, in agreement with the different ECSA, the mass activity increased from 307 A $g_{Pt}^{-1}$ for 34Pt/1Ta:$SnO_2$ to 465 A $g_{Pt}^{-1}$ for 7Pt/1Ta:$SnO_2$.

**Table 5.** Electrochemical specific surface area (ECSA), ORR mass activity (MA) and specific activity (SA) values obtained at 0.9 V *vs* RHE in 0.1 M $HClO_4$ for the different electrocatalysts before (BoT) and after the accelerated stress test consisting in 6,000 cycles from 1.0 to 1.6 V *vs* RHE (EoT).

| **Electrocatalyst** | **Pt loading (wt%)** | **ECSA BoT/[EoT] ($m^2$ $g^{-1}$)** | **MA BoT /[EoT] (A $g^{-1}$)** | **SA BoT /[EoT] (μA $cm^{-2}$)** |
|---|---|---|---|---|
| 34Pt/1Ta:$SnO_2$ | 34 | 48 ± 1/[30 ±1] | 307±11/[154±9] | 640±20/[513±25] |
| Pt/Vulcan | 30 | 80±2/[34±2] | 180±17/[65±16] | 225±15/[185±21] |
| commercial Pt/C | 57 | 78±1/[32±1] | 180±11/[90±10] | 231±20/[281±19] |
| 7Pt/1Ta:$SnO_2$ | 7 | 73±1/[59±1] | 465±9/[323±11] | 640±20/[538±16] |

Such high electrocatalytic activity can be attributed to two different phenomena: (i) Ta doping at 1 at.% may create oxygen vacancies in $SnO_2$ that could enhance the ORR activity [91]; (ii) the strong metal-support interaction between Pt and the doped metal oxide can modify the electronic structure of platinum with electron transfer from the support promoting the electrocatalysis [14,15,90,92]. The SMSI also induces lattice strain in the Pt nanoparticles deposited onto metal oxides with decrease in the activation energy for oxygen disassociation on their surface, and therefore enhancement in their ORR electrocatalytic activity [85].

We already demonstrated by an XPS study and discussed the SMSI effect on Pt on Sb:$SnO_2$ [15], and similar results were obtained in this work on Pt/Ta:$SnO_2$ (Table 4). Here the exceptional electroactivity enhancement, especially for the low loaded electrocatalysts (7Pt/1Ta:$SnO_2$), can be ascribed to the optimal metal loading, the Pt particle distribution and the electrical contact with the support.

In order to investigate the stability of the Ta:$SnO_2$ based electrocatalysts, an accelerated stress test (AST) at high voltage specifically designed to assess the support degradation was applied. The evolution of ECSA and ORR activity was monitored, and the corresponding results at beginning (BoT) and end of test (EoT) are shown in Table 5 and Figure 8.

After 6,000 cycles between 1.0 and 1.6 V *vs* RHE, the decay in electrochemical surface area (Figure 8b) and ORR activity (Figure S9 in Supporting Information and Table 5) was lower for the oxide-based than for the carbon-based electrodes, and in particular for the low-loaded Pt/Ta:$SnO_2$: ECSA loss of 37 % for 34Pt/1Ta:$SnO_2$ and of only 19 % for 7Pt/1Ta:$SnO_2$, *vs* 58 % for Pt/Vulcan and 60 % for HiSPEC 9100. This result is evidently due to the higher resistance to corrosion of the metal oxide support compared to carbon [12,15,16,24,29,30,40,89], as already demonstrated by the degradation test described above and the results depicted in Figure 5. The stability of the low-loaded Ta:$SnO_2$-based catalyst, similar to that recorded for 33Pt/Nb:$SnO_2$ [15], may also derive from a stronger interaction with the support (all particles are in contact with Ta:$SnO_2$ and no particle-particle interactions take place). The 7Pt/1Ta:$SnO_2$ electrocatalyst also demonstrated the higher retention of mass activity (70 %), while the MA of the other electrocatalyst was reduced by a factor of two. The exceptional mass activity and its retention after cycling at high potential of 7Pt/1Ta:$SnO_2$ could be ascribed to the higher interaction with Ta:$SnO_2$, leading to promoted electrocatalysis and stronger anchoring. XPS results indeed demonstrated a greater shift to lower binding energy of the Pt 4f peaks for the low loaded electrocatalyst (Figure 7a), highlighting the higher interaction and electronic transfer from tin oxide to the metal. 7 wt % represents the optimal Pt loading on a support of low surface area as 1Ta:$SnO_2$, allowing a homogeneous nanocatalyst distribution avoiding any metal nanoparticle-nanoparticle interaction

and improving electrical contact with the support, finally leading to high electrochemical activity and stability.

An accelerated stress test to characterize the Pt electrocatalyst degradation was performed with a reduced upper limit of 1.0 V *vs* RHE for 7Pt/1Ta:$SnO_2$. The decay in electrochemical surface area and in mass/specific activities were slightly lower (Table S2, Supporting Information) than those obtained at the end of the AST designed for degrading the support (up to 1.6 V *vs* RHE), suggesting that the instability was mainly driven by the Pt electrocatalyst than by Ta:$SnO_2$.

## 4. CONCLUSION

In $SnO_2$ fibers doped with different amounts of Ta, 1 at.% Ta doped tin oxide (1Ta:$SnO_2$) exhibited the highest electrical conductivity (0.09 $S \cdot cm^{-1}$) attributed to the structural distortion indicated by XRD, XPS and Raman spectroscopy. A very high ORR mass activity at 0.9 V *vs* RHE of 0.47 $A \cdot mg_{Pt}^{-1}$ was obtained for Pt/1Ta:$SnO_2$ with an ultra-low Pt loading (7 wt.%), to our knowledge the highest reported for metal oxide-supported electrocatalysts. In addition, electrochemical stability up to 1.6 V *vs* RHE was observed, with ECSA and mass activity retention of 81 and 70 %, respectively. These exceptional activity and stability amongst metal oxide supported catalysts were attributed to the strong interaction between Pt and Ta:$SnO_2$ for which XPS analysis provided evidence as well as to the high ECSA allowing for isolated nanoparticles well dispersed on the support. Improved synergy between support and catalyst leads to highly active and durable Ta:$SnO_2$-supported electrocatalysts, however the ultra-low platinum loading presents a challenge yet to be addressed in the preparation of functional cathode fuel cell catalyst layers.

ASSOCIATED CONTENT

**Supporting Information**. The Supporting Information is available free of charge on the ACS Publications website Relevant figures as noted in the text (PDF)

AUTHOR INFORMATION

**Corresponding Author**

*Sara Cavaliere, e-mail: sara.cavaliere@umontpellier.fr, tel: +33 4 67 14 90 98

**Author Contributions**

The manuscript was written through contributions of all authors. All authors have given approval to the final version of the manuscript.

‡These authors contributed equally.

**Supporting Information**

# Strong Interaction Between Platinum Nanoparticles and Tantalum Doped Tin Oxide Nanofibers and Its Activation and Stabilization Effect for Oxygen Reduction Reaction

*Ignacio Jiménez-Morales*[a, ‡], *Fatima Haidar*[a, ‡], *Sara Cavaliere*[a, b, *], *Deborah Jones*[a], *Jacques Rozière*[a]

[a] ICGM Université de Montpellier, CNRS, ENSCM, 34095 Montpellier Cedex 5, France.

[b] Institut Universitaire de France (IUF), 75231 Paris Cedex 5, France.

[*]Sara Cavaliere, e-mail: sara.cavaliere@umontpellier.fr, tel: +33 4 67 14 90 98

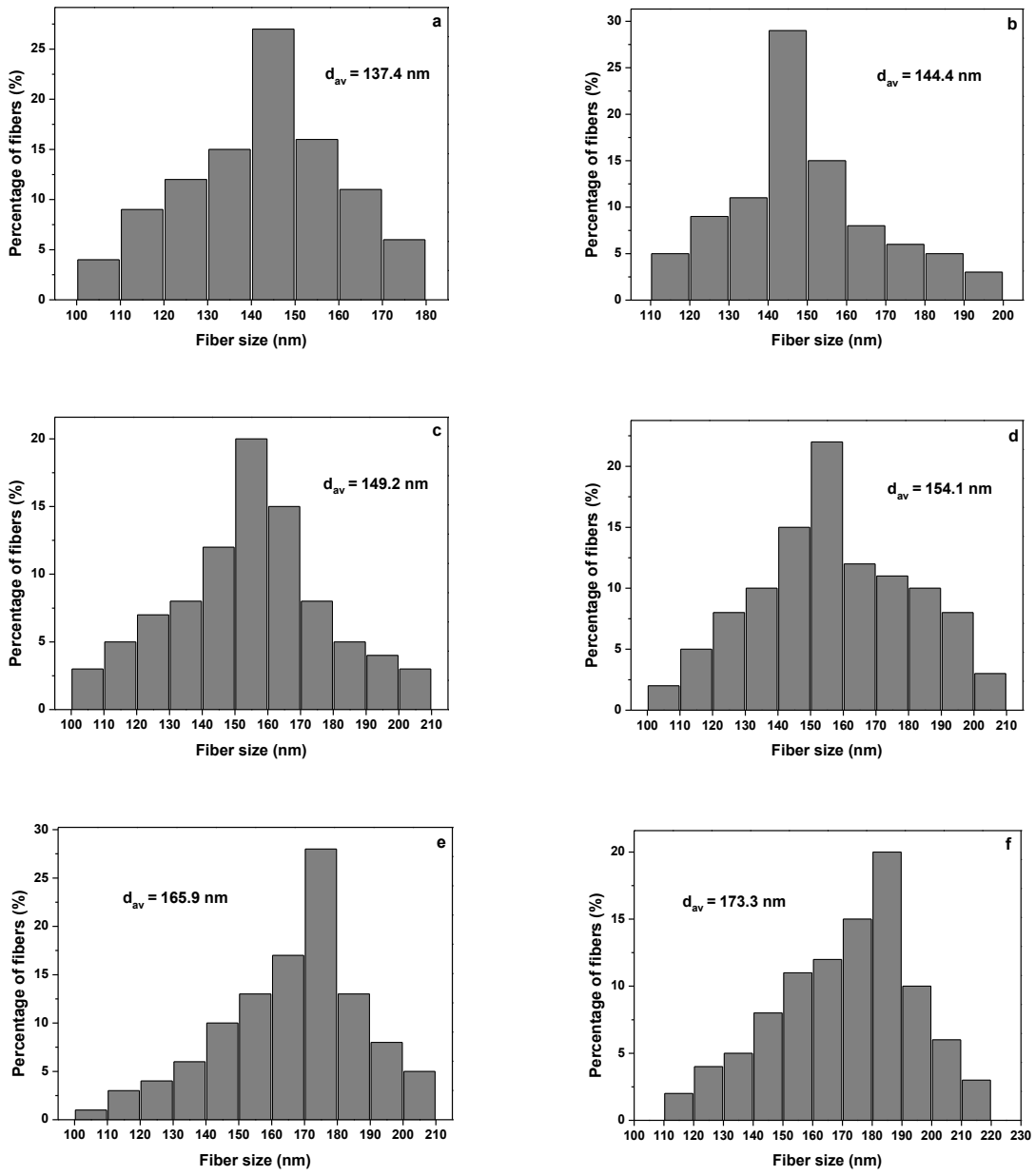


**Figure S1.** Fiber diameter distribution histograms of a) 0.5Ta:$SnO_2$, b) 1Ta:$SnO_2$, c) 1.5Ta:$SnO_2$, d) 2Ta:$SnO_2$, e) 5Ta:$SnO_2$ and f) 7.5Ta:$SnO_2$ from SEM images.

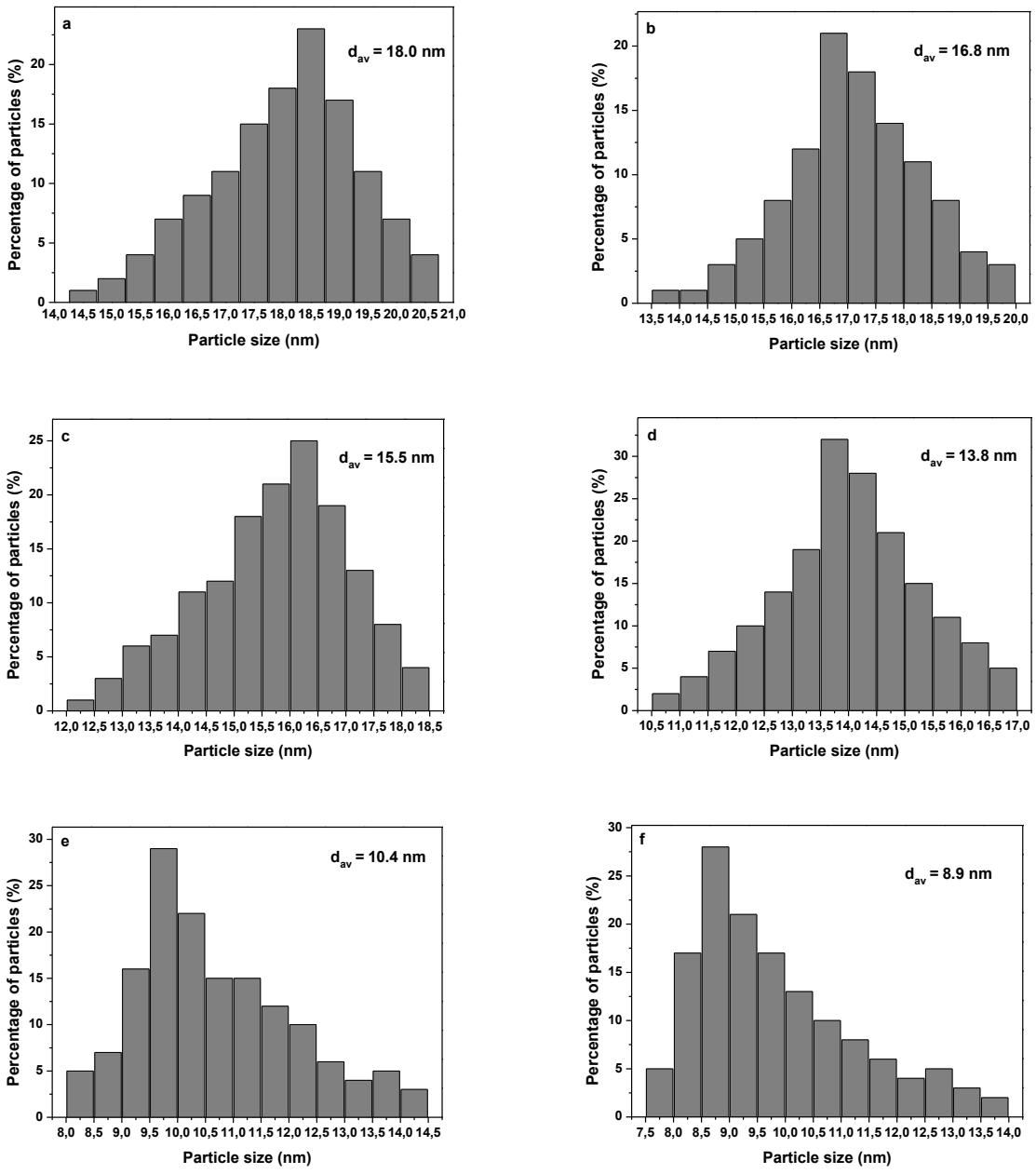


**Figure S2.** Particle size distribution histograms derived from TEM analysis of a) 0.5Ta:$SnO_2$, b) 1Ta:$SnO_2$, c) 1.5Ta:$SnO_2$, d) 2Ta:$SnO_2$ and e) 5Ta:$SnO_2$and f) 7.5 Ta:$SnO_2$.

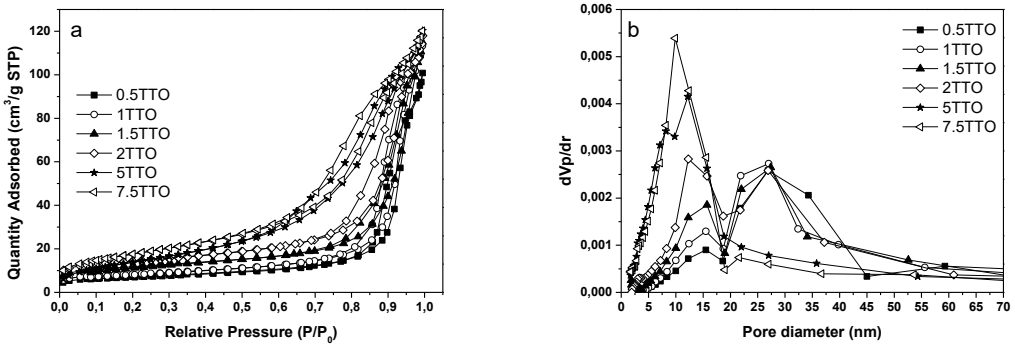


**Figure S3.** Nitrogen adsorption/desorption isotherms (a) and PSD (b) for Ta doped-$SnO_2$ electrospun materials.

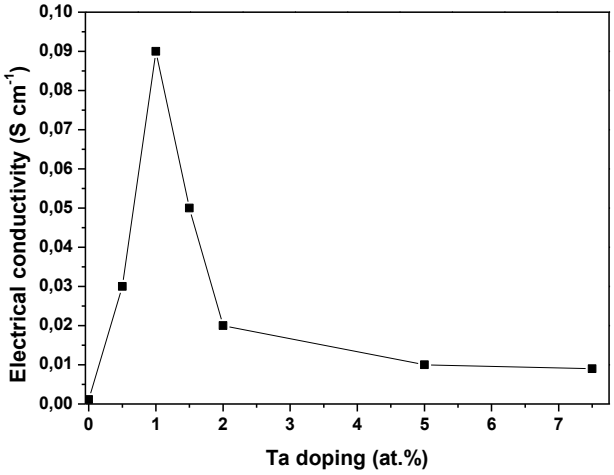


**Figure S4.** Electrical conductivity of tantalum doped $SnO_2$ electrospun materials.

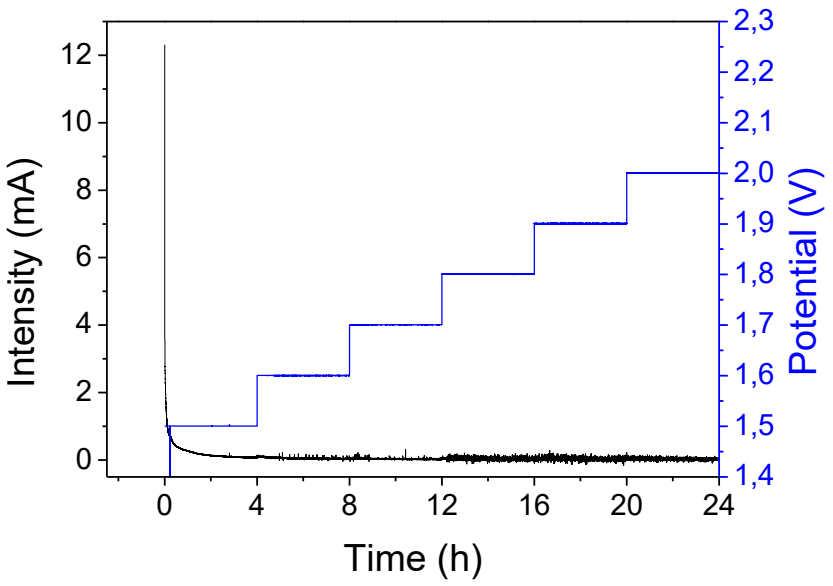


**Figure S5.** Chronoamperometry result on 1Ta:$SnO_2$ support at 1.5-2 V after every 4h step.

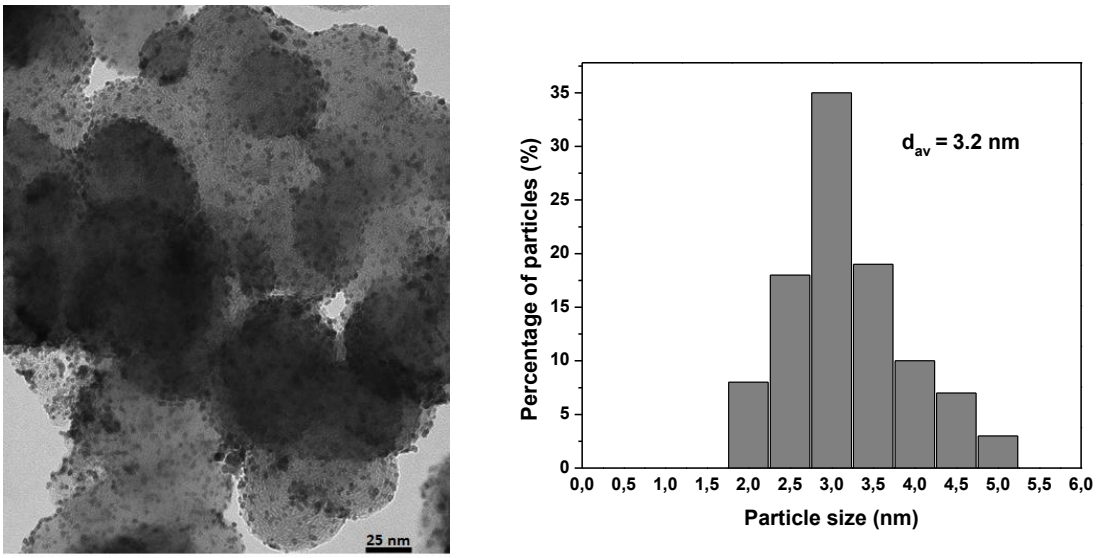


**Figure S6.** TEM micrograph of 30Pt/Vulcan and its corresponding Pt size distribution histogram.

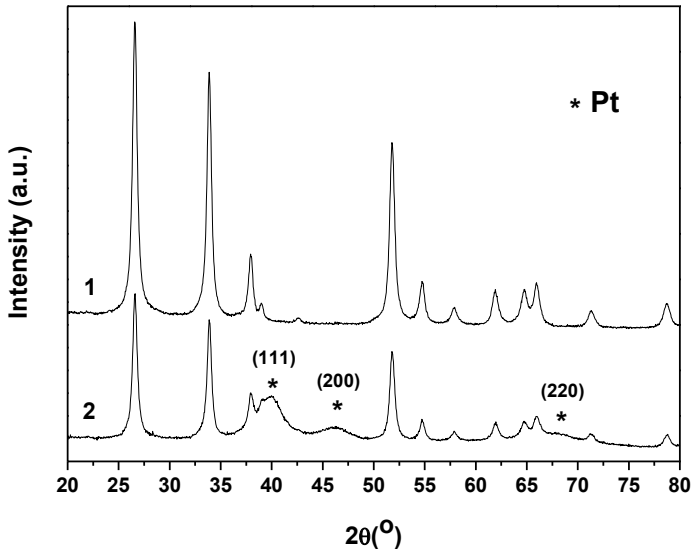


**Figure S7.** XRD diffractograms of 1Ta:$SnO_2$ (1) and 34Pt/1Ta:$SnO_2$ (2).

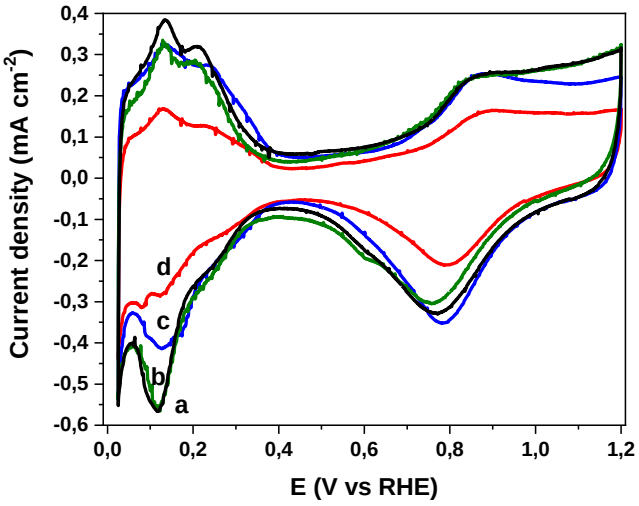


**Figure S8.** Cyclic voltammograms in $N_2$ saturated $HClO_4$ for a) 30Pt/Vulcan, b) commercial Pt/C, c) 7Pt/1Ta:$SnO_2$ and d) 34Pt/1Ta:$SnO_2$.

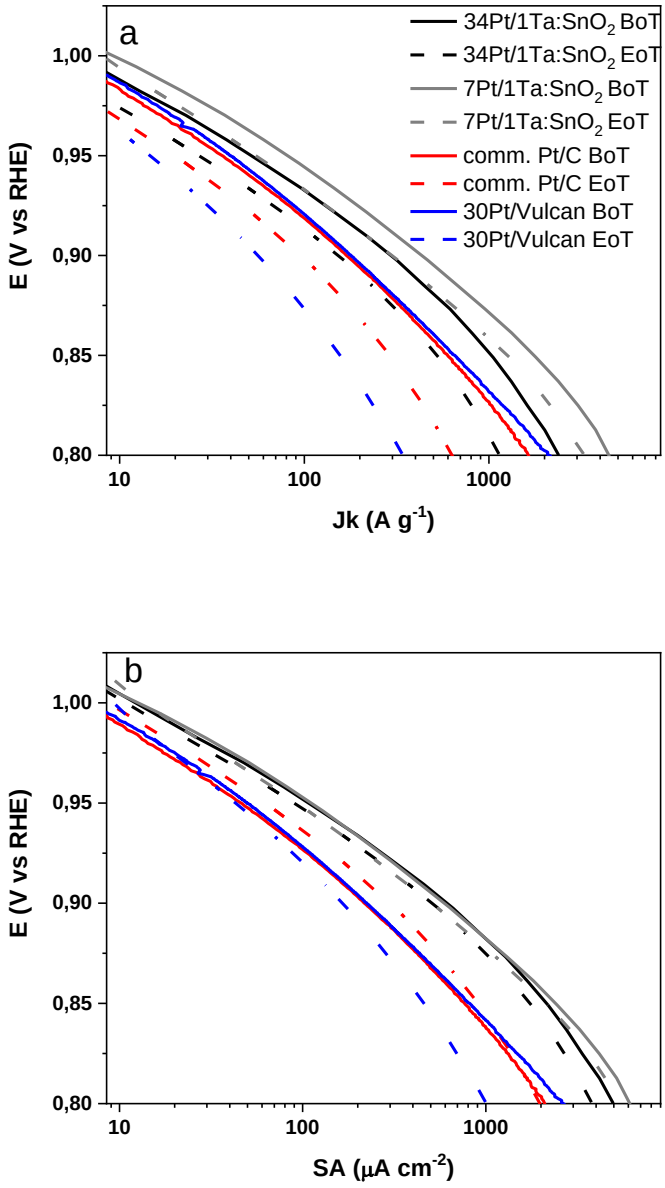


**Figure S9.** Tafel plots for the ORR mass (a) and specific activity for Pt nanoparticles deposited on 1Ta:$SnO_2$ (34 wt % Pt in black, 7 wt% in grey) and Vulcan (in blue) and for commercial Pt/C electrocatalyst (in red). The data were recorded at the beginning and end of the accelerated stress test (BoT, full lines, and EoT, dotted lines).

**Table S1.** Percentage of Ta and Sn elements leached from Ta:$SnO_2$ upon the indicated applied potentials.

| Applied potential (V) | Ta dissolved (wt%) | Sn dissolved (wt%) |
|---|---|---|
| 1.5 | 0.010 | 0.0019 |
| 1.6 | 0.015 | 0.0022 |
| 1.7 | 0.017 | 0.0028 |
| 1.8 | 0.019 | 0.0035 |
| 1.9 | 0.017 | 0.0045 |
| 2.0 | 0.018 | 0.0056 |
| **Total dissolved** | **0.10** | **0.021** |

**Table S2.** Electrochemical specific surface area (ECSA), ORR mass activity (MA) and specific activity (SA) values obtained at 0.9 V *vs* RHE in 0.1 M $HClO_4$ for the different electrocatalysts before (BoT) and after the accelerated stress test consisting in 10,000 cycles from 0.6 to 1.0 V *vs* RHE (EoT).

| Electrocatalyst | Pt loading (wt%) | ECSA BoT/[EoT] ($m^2$ $g^{-1}$) (0.6-1 V) | MA BoT /[EoT] (A $g^{-1}$) | SA BoT /[EoT] (μA $cm^{-2}$) |
|---|---|---|---|---|
| 7Pt/1Ta:$SnO_2$ | 7 | 73±1/[61±1] | 465±9/[354±11] | 640±20/[580±20.3] |

ACKNOWLEDGMENT

The research leading to these results has received funding from the European Research Council under the European Union's Seventh Framework Programme (FP/2007–2013)/ERC Grant Agreement SPINAM no. 306682 and from the French National Research Agency (ANR-17-CE05-0033 project MOISE, supported by Capenergies and Tenerrdis). SC acknowledges IUF for financial support.

REFERENCES

1. Ercolano, G.; Cavaliere, S.; Rozière, J.; Jones, D. J. Recent developments in electrocatalyst design thrifting noble metals in fuel cells. *Curr. Opin. Electrochem.* **2018**, *9*, 271–277.

2. Yu, Y.; Li, H.; Wang, H.; Yuan, X.-Z.; Wang, G.; Pan, M. A review on performance degradation of proton exchange membrane fuel cells during startup and shutdown processes: Causes, consequences, and mitigation strategies. *J. Power Sources* **2012**, *205*, 10–23.

3. Meier, J. C.; Galeano, C.; Katsounaros, I.; Topalov, A. A.; Kostka, A.; Schüth, F.; Mayrhofer, K. J. J. Degradation mechanisms of Pt/C fuel cell catalysts under simulated start-stop conditions. *ACS Catal.* **2012**, *2*, 832–843.

4. Wang, Y.-J.; Wilkinson, D. P.; Zhang, J. Noncarbon Support Materials for Polymer Electrolyte Membrane Fuel Cell Electrocatalysts. *Chem. Rev.* **2011**, *111*, 7625–7651.

5. Du, L.; Shao, Y.; Sun, J.; Yin, G.; Liu, J.; Wang, Y. Advanced catalyst supports for PEM fuel cell cathodes. *Nano Energy* **2016**, *29*, 314–322.

6. Shao, Y.; Liu, J.; Wang, Y.; Lin, Y. Novel catalyst support materials for PEMfuelcells: current status and future prospects. *J. Mater. Chem.* **2009**, *19*, 46–59.

7. Saha, M. S.; Neburchilov, V.; Ghosh, D.; Zhang, J. Nanomaterials-supported Pt catalysts for proton exchange membrane fuel cells. *Wiley Interdiscip. Rev. Energy Environ.* **2013**, *2*, 31–51.

8. Chhina, H.; Campbell, S.; Kesler, O. Ex situ Evaluation of Tungsten Oxide as a Catalyst Support for PEMFCs. *J. Electrochem. Soc.* **2007**, *154*, B533.

9. Chevallier, L.; Bauer, A.; Cavaliere, S.; Hui, R.; Rozière, J.; Jones, D. J. Mesoporous nanostructured Nb-doped titanium dioxide microsphere catalyst supports for PEM fuel cell electrodes. *ACS Appl. Mater. Interfaces* **2012**, *4*, 1752–1759.

10. Elezović, N.; Babić, B.; Gajić-Krstajić, L.; Radmilović, V.; Krstajić, N. V.; Vračar, L. J. Synthesis, characterization and electrocatalytical behavior of Nb–TiO2/Pt nanocatalyst for oxygen reduction reaction. *J. Power Sources* **2010**, *195*, 3961–3968.

11. Huang, S.-Y.; Ganesan, P.; Popov, B. N. Electrocatalytic activity and stability of niobium-doped titanium oxide supported platinum catalyst for polymer electrolyte membrane fuel cells. *Appl. Catal. B Environ.* **2010**, *96*, 224–231.

12. Savych, I.; Bernard d'Arbigny, J.; Subianto, S.; Cavaliere, S.; Jones, D. J.; Rozière, J. On the effect of non-carbon nanostructured supports on the stability of Pt nanoparticles during voltage cycling: A study of TiO2 nanofibres. *J. Power Sources* **2014**, *257*, 147–155.

13. Tauster, S. J. Strong metal-support interactions. *Acc. Chem. Res.* **1987**, *20*, 389–394.

14. Ma, J.; Habrioux, A.; Alonso-Vante, N. The Effect of Substrates at Cathodes in Low-temperature Fuel Cells. *ChemElectroChem* **2014**, *1*, 37–46.

15. Jiménez-Morales, I.; Cavaliere, S.; Jones, D.; Rozière, J. Strong metal–support interaction improves activity and stability of Pt electrocatalysts on doped metal oxides. *Phys. Chem. Chem. Phys.* **2018**, *20*, 8765–8772.

16. Takasaki, F.; Matsuie, S.; Takabatake, Y.; Noda, Z.; Hayashi, A.; Shiratori, Y.; Ito, K.; Sasaki, K. Carbon-Free Pt Electrocatalysts Supported on SnO2 for Polymer Electrolyte Fuel Cells: Electrocatalytic Activity and Durability. *J. Electrochem. Soc.* **2011**, *158*, B1270.

17. Sudan Saha, M.; Li, R.; Cai, M.; Sun, X. High Electrocatalytic Activity of Platinum Nanoparticles on SnO2 Nanowire-Based Electrodes. *Electrochem. Solid-State Lett.* **2007**, *10*, B130.

18. Stöwe, K.; Weber, M. Niobium, Tantalum, and Tungsten Doped Tin Dioxides as Potential Support Materials for Fuel Cell Catalyst Applications. *Zeitschrift für Anorg. und Allg. Chemie* **2020**, *646*, 1–12.

19. Chen, Y.; Wang, J.; Meng, X.; Zhong, Y.; Li, R.; Sun, X.; Ye, S.; Knights, S. Atomic layer deposition assisted Pt-SnO2 hybrid catalysts on nitrogen-doped CNTs with enhanced electrocatalytic activities for low temperature fuel cells. *Int. J. Hydrogen Energy* **2011**, *36*, 11085–11092.

20. Marichy, C.; Ercolano, G.; Caputo, G.; Willinger, M. G.; Jones, D.; Rozière, J.; Pinna, N.; Cavaliere, S. ALD SnO2 Protective Decoration Enhances the Durability of a Pt Based Electrocatalyst. *J. Mater. Chem. A* **2015**, *4*, 969–975.

21. Yang, D.; Sui, X.; Zhao, L.; Huang, G.; Gu, D.; Wang, Z. Pt Supported on Carbon-coating Antimony Tin Oxide as Anode Catalyst for Direct Methanol Fuel Cell. *Fuel Cells* **2018**, *18*, 763–

770.

22. Fu, Q.; Halck, N. B.; Hansen, H. A.; García Lastra, J. M.; Vegge, T. Computational Study of Nb-Doped-SnO 2 /Pt Interfaces: Dopant Segregation, Electronic Transport, and Catalytic Properties. *Chem. Mater.* **2017**, *29*, 1641–1649.

23. Senoo, Y.; Kakinuma, K.; Uchida, M.; Uchida, H.; Deki, S.; Watanabe, M. Improvements in electrical and electrochemical properties of Nb-doped SnO 2−δ supports for fuel cell cathodes due to aggregation and Pt loading. *RSC Adv.* **2014**, *4*, 32180.

24. Kakinuma, K.; Chino, Y.; Senoo, Y.; Uchida, M.; Kamino, T.; Uchida, H.; Deki, S.; Watanabe, M. Characterization of Pt catalysts on Nb-doped and Sb-doped SnO2–δ support materials with aggregated structure by rotating disk electrode and fuel cell measurements. *Electrochim. Acta* **2013**, *110*, 316–324.

25. Cognard, G.; Ozouf, G.; Beauger, C.; Jiménez-Morales, I.; Cavaliere, S.; Jones, D.; Rozière, J.; Chatenet, M.; Maillard, F. Pt Nanoparticles Supported on Niobium-Doped Tin Dioxide: Impact of the Support Morphology on Pt Utilization and Electrocatalytic Activity. *Electrocatalysis* **2017**, *8*, 51–58.

26. Ozouf, G.; Beauger, C. Niobium-and antimony-doped tin dioxide aerogels as new catalyst supports for PEM fuel cells. *J. Mater. Sci.* **2016**, *51*, 5305–5320.

27. Tsukatsune, T.; Takabatake, Y.; Noda, Z.; Daio, T.; Zaitsu, A.; Lyth, S. M.; Hayashi, A.; Sasaki, K. Platinum-Decorated Tin Oxide and Niobium-Doped Tin Oxide PEFC Electrocatalysts: Oxygen Reduction Reaction Activity. *J. Electrochem. Soc.* **2014**, *161*, F1208–F1213.

28. Savych, I.; Subianto, S.; Nabil, Y.; Cavaliere, S.; Jones, D.; Rozière, J. Negligible degradation

upon in situ voltage cycling of a PEMFC using an electrospun niobium-doped tin oxide supported Pt cathode. *Phys. Chem. Chem. Phys.* **2015**, *17*, 16970–16976.

29. Yin, M.; Xu, J.; Li, Q.; Jensen, J. O.; Huang, Y.; Cleemann, L. N.; Bjerrum, N. J.; Xing, W. Highly active and stable Pt electrocatalysts promoted by antimony-doped SnO2 supports for oxygen reduction reactions. *Appl. Catal. B Environ.* **2014**, *144*, 112–120.

30. Dou, M.; Hou, M.; Wang, F.; Liang, D.; Zhao, Q.; Shao, Z.; Yi, B. Sb-Doped SnO2 Supported Platinum Catalyst with High Stability for Proton Exchange Membrane Fuel Cells. *J. Electrochem. Soc.* **2014**, *161*, F1231–F1236.

31. Suffner, J.; Kaserer, S.; Hahn, H.; Roth, C.; Ettingshausen, F. Sb-doped SnO 2 hollow spheres offering micro- and nanoporosity in fuel cell electrode structures. *Adv. Energy Mater.* **2011**, *1*, 648–654.

32. Cognard, G.; Ozouf, G.; Beauger, C.; Dubau, L.; López-Haro, M.; Chatenet, M.; Maillard, F. Insights into the stability of Pt nanoparticles supported on antimony-doped tin oxide in different potential ranges. *Electrochim. Acta* **2017**, *245*, 993–1004.

33. Ozouf, G.; Cognard, G.; Maillard, F.; Chatenet, M.; Guétaz, L.; Heitzmann, M.; Jacques, P. A.; Beauger, C. Sb-Doped SnO $_2$ Aerogels Based Catalysts for Proton Exchange Membrane Fuel Cells: Pt Deposition Routes, Electrocatalytic Activity and Durability. *J. Electrochem. Soc.* **2018**, *165*, F3036–F3044.

34. Mohanta, P. K.; Glökler, C.; Arenas, A. O.; Jörissen, L. Sb doped SnO2 as a stable cathode catalyst support for low temperature polymer electrolyte membrane fuel cell. *Int. J. Hydrogen Energy* **2017**, *2*, 1–12.

35. Chen, S. Fine-tuning the Cross-Sectional Architecture of Antimony- doped Tin Oxide Nanofibers as Pt Catalyst Support for Enhanced Oxygen Reduction Activity. *Int. J. Electrochem. Sci.* **2017**, *12*, 6221–6231.

36. Fabbri, E.; Rabis, A.; Kötz, R.; Schmidt, T. J. Pt nanoparticles supported on Sb-doped SnO2 porous structures: developments and issues. *Phys. Chem. Chem. Phys.* **2014**, *16*, 13672–81.

37. Cavaliere, S.; Jiménez-Morales, I.; Ercolano, G.; Savych, I.; Jones, D.; Rozière, J. Highly Stable PEMFC Electrodes Based on Electrospun Antimony-Doped SnO2. *ChemElectroChem* **2015**, *2*, 1966–1973.

38. Elezovic, N. R.; Radmilovic, V. R.; Kovac, J.; Babic, B. M.; Gaijic-Krstajic, L. M.; Krstajic, N. V. Pt nanoparticles on tin oxide based support as a beneficial catalyst for oxygen reduction in alkaline solutions. *RSC Adv.* **2015**, *5*, 15923–15929.

39. Liu, G.; Xu, J.; Wang, Y.; Wang, X. An oxygen evolution catalyst on an antimony doped tin oxide nanowire structured support for proton exchange membrane liquid water electrolysis. *J. Mater. Chem. A* **2015**, *3*, 20791–20800.

40. Rodríguez-García, B.; Reyes-Carmona, Á.; Jiménez-Morales, I.; Blasco-Ahicart, M.; Cavaliere, S.; Dupont, M.; Jones, D.; Rozière, J.; Galán-Mascarós, J. R.; Jaouen, F. Cobalt hexacyanoferrate supported on Sb-doped SnO2 as a non-noble catalyst for oxygen evolution in acidic medium. *Sustain. Energy Fuels* **2018**, *2*, 589–597.

41. Geiger, S.; Kasian, O.; Mingers, A. M.; Mayrhofer, K. J. J.; Cherevko, S. Stability limits of tin-based electrocatalyst supports. *Sci. Rep.* **2017**, *7*, 3–9.

42. Wang, Y.; Brezesinski, T.; Antonietti, M.; Smarsly, B. Ordered Mesoporous Sb-, Nb-, and Ta-

Doped SnO 2 Thin Films with Adjustable Doping Levels and High Electrical Conductivity. *ACS Nano* **2009**, *3*, 1373–1378.

43. Senoo, Y.; Taniguchi, K.; Kakinuma, K.; Uchida, M.; Uchida, H.; Deki, S.; Watanabe, M. Cathodic performance and high potential durability of Ta-SnO2-δ-supported Pt catalysts for PEFC cathodes. *Electrochem. commun.* **2015**, *51*, 37–40.

44. Takahashi, K.; Kakinuma, K.; Uchida, M. Improvement of Cell Performance in Low-Pt-Loading PEFC Cathode Catalyst Layers Prepared by the Electrospray Method. *J. Electrochem. Soc.* **2016**, *163*, F1182–F1188.

45. Takahashi, K.; Koda, R.; Kakinuma, K.; Uchida, M. Improvement of Cell Performance in Low-Pt-Loading PEFC Cathode Catalyst Layers with Pt/Ta-SnO 2 Prepared by the Electrospray Method. *J. Electrochem. Soc.* **2017**, *164*, F235–F242.

46. Solà-Hernández, L.; Claudel, F.; Maillard, F.; Beauger, C. Doped tin oxide aerogels as oxygen evolution reaction catalyst supports. *Int. J. Hydrogen Energy* **2019**, *44*, 24331–24341.

47. Dubau, L.; Maillard, F.; Chatenet, M.; Cavaliere, S.; Jiménez-Morales, I.; Mosdale, A.; Mosdale, R. Durability of Alternative Metal Oxide Supports for Application at a Proton-Exchange Membrane Fuel Cell Cathode—Comparison of Antimony- and Niobium-Doped Tin Oxide. *Energies* **2020**, *13*, 403.

48. Jiménez-Morales, I.; Cavaliere, S.; Dupont, M.; Jones, D.; Rozière, J. On the stability of antimony doped tin oxide supports in proton exchange membrane fuel cell and water electrolysers. *Sustain. Energy Fuels* **2019**, *3*, 1526–1535.

49. Cavaliere, S.; Subianto, S.; Savych, I.; Tillard, M.; Jones, D. J.; Rozière, J.; Jones, D. J. Dopant-

Driven Nanostructured Loose-Tube SnO2 Architectures: Alternative Electrocatalyst Supports for Proton Exchange Membrane Fuel Cells. *J. Phys. Chem. C* **2013**, *117*, 18298–18307.

50. Larsen, M. J.; Jiménez Morales, I.; Cavaliere, S.; Zajac, J.; Jones, D. J.; Rozière, J.; Kaluža, L.; Gulková, D.; Odgaard, M. Development of tailored high-performance and durable electrocatalysts for advanced PEM fuel cells. *Int. J. Hydrogen Energy* **2017**.

51. Kocha, S. S.; Garsany, Y.; Myers, D. Testing Oxygen Reduction Reaction Activity with the Rotating Disc Electrode Technique. *DOE Webinar* **2013**.

52. Senthilkumar, V.; Vickraman, P.; Jayachandran, M.; Sanjeeviraja, C. Structural and electrical studies of nano structured Sn1−x Sb x O2 (x = 0.0, 1, 2.5, 4.5 and 7 at%) prepared by co-precipitation method. *J. Mater. Sci. Mater. Electron.* **2009**, *21*, 343–348.

53. Zyubin, A. S.; Zyubina, T. S.; Dobrovol'skii, Y. A.; Frolova, L. A.; Volokhov, V. M. Platinum nanoparticles on the antimony-doped tin dioxide surface: Quantum-chemical modeling. *Russ. J. Inorg. Chem.* **2013**, *58*, 1489–1495.

54. Leite, B. E. R.; Weber, I. T.; Longo, E.; Varela, J. A. A New Method to Control Particle Size and Particle Size Distribution of SnO2 Nanoparticles for Gas Sensor Applications. *Adv. Mater.* **2000**, *12*, 965–968.

55. Jiménez-Morales, I.; Moreno-Recio, M.; Santamaría-González, J.; Maireles-Torres, P.; Jiménez-López, A. Mesoporous tantalum oxide as catalyst for dehydration of glucose to 5-hydroxymethylfurfural. *Appl. Catal. B Environ.* **2014**, *154–155*, 190–196.

56. Jiménez-Morales, I.; Santamaría-González, J.; Maireles-Torres, P.; Jiménez-López, A. Methanolysis of sunflower oil catalyzed by acidic Ta2O5 supported on SBA-15. *Appl. Catal. A*

*Gen.* **2011**, *405*, 93–100.

57. Katiyar, R. S.; Dawson, P.; Hargreave, M. M.; Wilkinson, G. R. Dynamics of the rutile structure 111 . Lattice dynamics , infrared and Raman spectra of SnO ,. *J. Phys. C Solid State Phys.* **1971**, *4*, 2421–2431.

58. Chang, S. S.; Jo, M. S. Luminescence properties of Eu-doped SnO2. *Ceram. Int.* **2007**, *33*, 511–514.

59. Jiang, Z.; Guo, Z.; Sun, B.; Jia, Y.; Li, M.; Liu, J. Highly sensitive and selective butanone sensors based on cerium-doped SnO2thin films. *Sensors Actuators, B Chem.* **2010**, *145*, 667–673.

60. Wang, Y.; Aponte, M.; Leon, N.; Ramos, I.; Furlan, R.; Pinto, N.; Evoy, S.; Santiago-Avilés, J. J. Synthesis and Characterization of Ultra-Fine Tin Oxide Fibers Using Electrospinning. *J. Am. Ceram. Soc.* **2005**, *88*, 2059–2063.

61. Wang, W.; Xu, C.; Wang, G.; Liu, Y.; Zheng, C. Synthesis and Raman scattering study of rutile SnO2 nanowires. *J. Appl. Phys.* **2002**, *92*, 2740–2742.

62. Singh, G.; Singh, R. C. Synthesis and characterization of Gd-doped SnO2 nanostructures and their enhanced gas sensing properties. *Ceram. Int.* **2017**, *43*, 2350–2360.

63. Liu, L. Z.; Li, T. H.; Wu, X. L.; Shen, J. C.; Chu, P. K. Identification of oxygen vacancy types from Raman spectra of SnO2nanocrystals. *J. Raman Spectrosc.* **2012**, *43*, 1423–1426.

64. Diéguez, A.; Romano-Rodríguez, A.; Vilà, A.; Morante, J. R. The complete Raman spectrum of nanometric SnO2particles. *J. Appl. Phys.* **2001**, *90*, 1550–1557.

65. Costa, I. M.; Colmenares, Y. N.; Pizani, P. S.; Leite, E. R.; Chiquito, A. J. Sb doping of VLS

synthesized SnO2nanowires probed by Raman and XPS spectroscopy. *Chem. Phys. Lett.* **2018**, *695*, 125–130.

66. Bonu, V.; Das, A.; Sivadasan, A. K.; Tyagi, A. K.; Dhara, S. Invoking forbidden modes in SnO 2 nanoparticles using tip enhanced Raman spectroscopy. *J. Raman Spectrosc.* **2015**, *46*, 1037–1040.

67. Sing, K. S. W.; Everett, D. H.; Haul, R. A. W.; Moscou, L.; Pierotti, R. A.; Rouquérol, J.; Siemieniewska, T. Reporting physisorption data for gas/solid systems with special reference to the determination of surface area and porosity (Recommendations 1984). *Pure Appl. Chem.* **1985**, *57*, 603–619.

68. Ben Soltan, W.; Mbarki, M.; Ammar, S.; Babot, O.; Toupance, T. Structural and optical properties of vanadium doped SnO2nanoparticles synthesized by the polyol method. *Opt. Mater. (Amst).* **2016**, *54*, 139–146.

69. Vo, T. T. X.; Le, T. N. H.; Pham, Q. N.; Byl, C.; Dragoe, D.; Barthés-Labrousse, M. G.; Bérardan, D.; Dragoe, N. Preparation and study of the thermoelectric properties of nanocrystalline Sn1-xTaxO2 ($0 \leq x \leq 0.04$). *Phys. Status Solidi Appl. Mater. Sci.* **2015**, *212*, 2776–2784.

70. Liu, Q.; Zhang, L.; Chen, J.-F.; Le, Y. Synthesis of TiO2@ATO core–shell nanofibers using coaxial electrospinning. *Mater. Lett.* **2014**, *137*, 339–342.

71. Lee, S. W.; Kim, Y.-W.; Chen, H. Electrical properties of Ta-doped SnO2 thin films prepared by the metal–organic chemical-vapor deposition method. *Appl. Phys. Lett.* **2001**, *78*, 350–352.

72. Husain, S.; Akansel, S.; Kumar, A.; Svedlindh, P.; Chaudhary, S. Growth of Co2 FeAl Heusler alloy thin films on Si(100) having very small Gilbert damping by Ion beam sputtering. *Sci. Rep.*

**2016**, *6*.

73. Weidner, M. Fermi Level Determination in Tin Oxide by Photoelectron Spectroscopy: Relation to Optoelectronic Properties; Band Bending at Surfaces and Interfaces; Modulation Doping. **2016**, 361.

74. Montilla, F.; Morallón, E.; De Battisti, A.; Barison, S.; Daolio, S.; Vázquez, J. L. Preparation and characterization of antimony-doped tin dioxide electrodes. 3. XPS and SIMS characterization. *J. Phys. Chem. B* **2004**, *108*, 15976–15981.

75. Bomben, K. D.; Moulder, J. F.; Sobol, P. E.; Stickle, W. F. *Handbook of x-ray photoelectron spectroscopy. A reference bookof standard spectra for identification and interpretation of xpsdata.*; Physical Electronics: Eden Prairie, MN, 1995.

76. Worsdale, M.; Rabis, A.; Fabbri, E.; Schmidt, T. J.; Kramer, D. Conductivity Limits of Extrinsically Doped SnO2 Supports. *ECS Trans.* **2015**, *69*, 1167–1178.

77. Geiger, S.; Kasian, O.; Mingers, A. M.; Nicley, S. S.; Haenen, K.; Mayrhofer, K. J. J.; Cherevko, S. Catalyst Stability Benchmarking for the Oxygen Evolution Reaction: The Importance of Backing Electrode Material and Dissolution in Accelerated Aging Studies. *ChemSusChem* **2017**, *10*, 4140–4143.

78. Raynal, F.; Etcheberry, A.; Cavaliere, S.; Noël, V.; Perez, H. Characterization of the unstability of 4-mercaptoaniline capped platinum nanoparticles solution by combining LB technique and X-ray photoelectron spectroscopy. *Appl. Surf. Sci.* **2006**, *252*, 2422–2431.

79. Ioannides, T.; Verykios, X. E. Charge transfer in metal catalysts supported on doped TiO2: A theoretical approach based on metal-semiconductor contact theory. *J. Catal.* **1996**, *161*, 560–569.

80. Fu, Q.; Wagner, T.; Olliges, S.; Carstanjen, H. D. Metal-oxide interfacial reactions: Encapsulation of Pd on TiO2 (110). *J. Phys. Chem. B* **2005**, *109*, 944–951.

81. Figueiredo, W. T.; Della Mea, G. B.; Segala, M.; Baptista, D. L.; Escudero, C.; Pérez-Dieste, V.; Bernardi, F. Understanding the Strong Metal-Support Interaction (SMSI) Effect in CuxNi1-x/CeO2 (0 < x < 1) Nanoparticles for Enhanced Catalysis. *ACS Appl. Nano Mater.* **2019**, *2*, 2559–2573.

82. Rabis, A.; Binninger, T.; Fabbri, E.; Schmidt, T. J. Impact of Support Physicochemical Properties on the CO Oxidation and the Oxygen Reduction Reaction Activity of Pt/SnO2 Electrocatalysts. *J. Phys. Chem. C* **2018**, *122*, 4739–4746.

83. Kakinuma, K.; Suda, K.; Kobayashi, R.; Tano, T.; Arata, C.; Amemiya, I.; Watanabe, S.; Matsumoto, M.; Imai, H.; Iiyama, A.; Uchida, M. Electronic States and Transport Phenomena of Pt Nanoparticle Catalysts Supported on Nb-Doped SnO2 for Polymer Electrolyte Fuel Cells. *ACS Appl. Mater. Interfaces* **2019**, *11*, 34957–34963.

84. Ando, F.; Tanabe, T.; Gunji, T.; Tsuda, T.; Kaneko, S.; Takeda, T.; Ohsaka, T.; Matsumoto, F. Improvement of ORR Activity and Durability of Pt Electrocatalyst Nanoparticles Anchored on TiO 2 /Cup-Stacked Carbon Nanotube in Acidic Aqueous Media. *Electrochim. Acta* **2017**, *232*, 404–413.

85. Daio, T.; Staykov, A.; Guo, L.; Liu, J.; Tanaka, M.; Matthew Lyth, S.; Sasaki, K. Lattice Strain Mapping of Platinum Nanoparticles on Carbon and SnO 2 Supports. *Sci. Rep.* **2015**, *5*, 1–10.

86. Chikunova, I. O.; Semeykina, V. S.; Kuznetsov, A. N.; Kalinkin, P. N.; Gribov, E. N.; Parkhomchuk, E. V. Template-assisted synthesis and electrochemical properties of SnO2 as a

cathode catalyst support for PEMFC. *Ionics (Kiel).* **2019**.

87. Mohamed, R.; Binninger, T.; Kooyman, P. J.; Hoell, A.; Fabbri, E.; Patru, A.; Heinritz, A.; Schmidt, T. J.; Levecque, P. Facile deposition of Pt nanoparticles on Sb-doped SnO2 support with outstanding active surface area for the oxygen reduction reaction. *Catal. Sci. Technol.* **2018**, *8*, 2672–2685.

88. Cognard, G.; Ozouf, G.; Beauger, C.; Berthomé, G.; Riassetto, D.; Dubau, L.; Chattot, R.; Chatenet, M.; Maillard, F. Benefits and limitations of Pt nanoparticles supported on highly porous antimony-doped tin dioxide aerogel as alternative cathode material for proton-exchange membrane fuel cells. *Appl. Catal. B Environ.* **2017**, *201*, 381–390.

89. Elezovic, N. R.; Babic, B. M.; Radmilovic, V. R.; Krstajic, N. V. Synthesis and Characterization of Pt Catalysts on SnO2 Based Supports for Oxygen Reduction Reaction. *J. Electrochem. Soc.* **2013**, *160*, F1151–F1158.

90. de la Pena O'Shea, V. A.; Alvarez Galvan, M. C.; Platero Prats, A. E.; Campos-Martin, J.; Fierro, J. Direct evidence of the SMSI decoration effect : the case of Co/TiO2 catalyst. *Chem. Commun. (Camb).* **2011**, *47*, 7131–7133.

91. Alegre, C.; Siracusano, S.; Modica, E.; Aricò, A. S.; Baglio, V. Titanium–tantalum oxide as a support for Pd nanoparticles for the oxygen reduction reaction in alkaline electrolytes. *Mater. Renew. Sustain. Energy* **2018**, *7*, 1–10.

92. Xiong, L.; Manthiram, A. Synthesis and characterization of methanol tolerant Pt/TiOx/C nanocomposites for oxygen reduction in direct methanol fuel Cells. *Electrochim. Acta* **2004**, *49*, 4163–4170.